

2016

Investigation of momentum exchange term closures for the Eulerian-Eulerian model applied to bubbly flows

Hao Bai
Iowa State University

Follow this and additional works at: <https://lib.dr.iastate.edu/etd>



Part of the [Chemical Engineering Commons](#), and the [Mechanical Engineering Commons](#)

Recommended Citation

Bai, Hao, "Investigation of momentum exchange term closures for the Eulerian-Eulerian model applied to bubbly flows" (2016). *Graduate Theses and Dissertations*. 15871.
<https://lib.dr.iastate.edu/etd/15871>

This Thesis is brought to you for free and open access by the Iowa State University Capstones, Theses and Dissertations at Iowa State University Digital Repository. It has been accepted for inclusion in Graduate Theses and Dissertations by an authorized administrator of Iowa State University Digital Repository. For more information, please contact digirep@iastate.edu.

Investigation of momentum exchange term closures for the Eulerian-Eulerian model applied to bubbly flows

by

Hao Bai

A thesis submitted to the graduate faculty
in partial fulfillment of the requirements for the degree of

MASTER OF SCIENCE

Major: Mechanical Engineering

Program of Study Committee:
Alberto Passalacqua, Major Professor
Rodney O Fox
Theodore Heindel

Iowa State University

Ames, Iowa

2016

Copyright © Hao Bai, 2016. All rights reserved.

TABLE OF CONTENTS

ACKNOWLEDGMENTS	v
ABSTRACT.....	vi
CHAPTER 1. INTRODUCTION.....	1
1.1. Motivation.....	1
1.2. Objective.....	2
1.3. Literature Review.....	2
1.4. Outline.....	7
CHAPTER 2. THEORY AND EQUATIONS.....	8
2.1. Two-Fluid Model.....	8
2.2. Drag Model.....	9
2.3. Lift Model.....	11
2.4. Virtual Mass.....	14
2.5. Wall Lubrication.....	14
2.6. Bubble Dispersion Force.....	16
CHAPTER 3. PSEUDO 2D RECTANGULAR BUBBLE COLUMN.....	18
3.1. Experimental Overview.....	18
3.2. Mesh Convergence Test.....	19

3.3. Sub-Model Accuracy Tests	23
3.3.1. Drag correlation tests	23
3.3.2. Lift force tests	32
3.3.3. Wall lubrication force tests	39
3.3.4. Conclusions and future work	45
3.4. Stability Analysis in the 2D Rectangular Bubble Column.....	46
3.4.1. Case review	47
3.4.2. Conclusions.....	51
3.5. Comparisons of 2D and 3D Simulations of the Rectangular Bubble Column	52
3.5.1. Case setup	52
3.5.2. Comparison of 2D and 3D simulation results.....	53
3.5.3 Conclusions.....	61
CHAPTER 4. CYLINDRICAL BUBBLE COLUMN	63
4.1. Experimental Overview	63
4.2. Mesh Convergence Test for the Cylindrical Bubble Column.....	65
4.3. Stability Analysis of the Cylinder Bubble Column	72
4.3.1. Experimental overview of the cylinder bubble column stability	72
4.3.2. Cylinder bubble column stability analysis in OpenFOAM	73
4.3.3. Conclusion	80

4.4. Validation of Bubble Dispersion Force in the Two-Fluid Model.....	80
4.4.1. Case setup	81
4.4.2. Cylindrical bubble column analysis	82
4.4.3. Validation of the bubble dispersion force for the Pflieger case.....	87
4.4.4. Conclusion	93
CHAPTER 5. CONCLUSION.....	94
5.1. Investigating the 2D Rectangular Bubble Column	94
5.2. Investigating the Cylindrical Bubble Column	94
5.3. Future Work.....	95
REFERENCES	96

ACKNOWLEDGMENTS

I would like to thank my advisor, Prof. Alberto Passalacqua, and my committee members, Prof. Rodney O. Fox and Prof. Ted Heindel, for their guidance and support throughout the course of this research project.

In addition, I would also like to thank my friends, colleagues, the department faculty and staff for making my time at Iowa State University a wonderful experience.

ABSTRACT

The objective of the work presented in this thesis was to improve the accuracy of the two-fluid model for simulating flow behavior in bubble columns. To achieve this investigation, computational fluid dynamics (CFD) simulations were conducted using the open source software OpenFOAM[®] and compared to the experimental results of Harteveld (2005).

The CFD simulations were performed using the two-fluid solver in OpenFOAM, which describes the phases as interpenetrating continua, identified by the corresponding phase volume fractions. Several models for drag, lift, virtual mass, and wall-lubrication were validated in the presented work. The following objectives were accomplished in order to achieve the final goal. First, different drag, lift, wall lubrication, and virtual mass models were applied to the two-fluid model to test its accuracy for a 2D rectangular bubble column. Next, OpenFOAM simulations of a 3D rectangular bubble column were performed using the pre-tested sub-models. The resulting flow behavior was compared to previous 2D simulations and experimental results. Finally, the stability of the 2D rectangular bubble column was investigated.

After fully studying rectangular bubble column simulations, a 3D cylindrical bubble column was subsequently simulated. An investigation of the mesh independence was performed and simulation results were compared to experimental data. Finally, an analysis of the 3D cylindrical bubble column stability was conducted by changing the inject velocities.

CHAPTER 1. INTRODUCTION

1.1. Motivation

Multi-phase gas-liquid flows have frequently been used in the chemical, biological, nuclear, and petrochemical industries. Most of these systems use buoyancy-driven flows. Bubble column reactors are widely used for chemical processes due to their simple construction, low maintenance and operation costs, and high efficiency in terms of mass and heat transfer (Jakobsen, 2009). The simplest form of a bubble column reactor is a vertical cylinder that is filled with liquid and can be injected with gas from the bottom, side, or even top of the column.

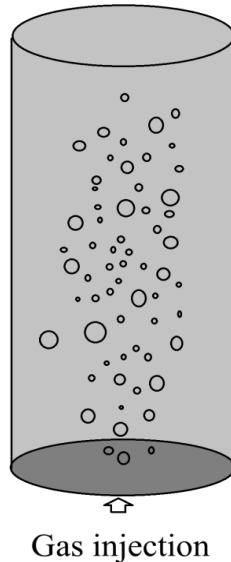


Fig. 1. The simple geometry of a bubble column.

Fig. 1 provides a basic diagram of a bubble column reactor featuring gas injection from the bottom. As the bubbles flow upward, some amount of the liquid that surrounds each bubble follows its path. Thus, large bubbles and liquid rise together near the center of the bubble column, and in order to satisfy the conservation of mass, liquid must also flow downwards along the walls (Jakobsen, 2009). The objective of the bubble column reactor is to create a uniform bubble

size that can maximize the bubble surface area between the gas and liquid phases. To achieve this objective, researchers have conducted many studies of bubble columns using both experimental means and computational fluid dynamics (CFD) simulations. A good CFD study of a bubble column can help predict flow behavior inside the reactor.

1.2. Objective

The objective of this work was to use the open-source software OpenFOAM to simulate different flow behaviors inside various bubble column geometries and to investigate and determine the effects of different forces, including drag, lift, virtual mass, and wall lubrication, on bubbly flows. The goal is to understand how dynamic large-scale fluctuation happens in bubble column reactors at various scales and at different superficial velocities of gas injection. This study also aimed to investigate the effects of inlet patterns on large-scale fluctuation inside bubble columns. These goals were completed by simulating 2D rectangular bubble columns with different inlet patterns based on experiments conducted by Hartevelde (2005) and comparing the flow behavior observed in CFD simulation to those prior experimental results. In addition, a large-scale 3D bubble column was simulated based on other experiments by Hartevelde (2005) to perform a stability analysis, which gave a range of superficial gas velocities at which the large-scale fluctuation started to show.

1.3. Literature Review

To design bubble column reactors, researchers need detailed knowledge of the hydrodynamics of multiphase gas-liquid flows. CFD is well situated to provide detailed understanding of the physical phenomena of the hydrodynamics within bubble column reactors.

Researchers widely use the two-fluid model, or averaged Euler-Euler model, for simulating gas-liquid flows. The flow behavior is described and solved using the continuity and momentum equations, which do not contain any detailed flow, but rather rely on process averages (Drew, 1982). The accuracy of the two-fluid model strongly depends on the selection of sub-models, such as drag, lift, virtual mass, wall lubrication, and bubble-induced turbulence (Drew, 1982).

Since bubbles in liquid are mainly buoyancy driven, the drag force is the most important force acting on them, and it acts in the opposite direction of the bubble's movement. Therefore, many studies concentrate on this drag effect. According to Tomiyama et al. (1998), for a single bubble flowing up in a pipe, the drag force highly depends on the bubble's diameter, the difference in density between the two phases, and the gravitational force. Tomiyama uses the Eötvös number to describe the ratio of the buoyancy force to the surface tension of the bubble, which helps define the shape of the bubble in the liquid phase. Tomiyama et al.'s (1998) results were obtained at a range of Eötvös, Morton, and Reynolds numbers. Another drag law, studied by Tenneti et al. (2011), employs the Particle-resolved Uncontaminated-fluid Reconcilable Immersed Boundary Method to complete the Particle-resolved Direct Numerical Simulation. The drag correlation, proposed by Tenneti et al. (2011) is applied in the momentum equations to test the model accuracy.

In Tomiyama (1998), the author also provided a lift model for bubbly flow. A 3D one-way bubble tracking method was used to predict the upward flow of bubbles in a vertical pipe and a two-fluid model was used to determine the bubble distribution in the pipe. Another study for lift force was described in Legendre and Magnaudet (1998) who proposed the Legendre and Magnaudet lift model, which concludes that the bubbly flow in a liquid depends on the Reynolds

number and the shear rate. The authors derived the model for non-distorted bubbles, and in this thesis bubble diameter is assumed to be constant, and thus the Legendre and Magnaudet model can be applied to this work. Moraga et al. (1999) determined the time averaged magnitude of the forces using a static force balance of drag, lift and buoyancy, also proposing a lift model for the two-fluid model.

Some studies found that when bubbles are close to but not touching the wall that the wall lubrication force may be observed. For example, Antal et al. (1991) uses the two-fluid model to predict bubble distribution in a cylinder pipe for laminar flow and found lift and wall lubrication forces affected the void fraction profile. The Tomiyama wall lubrication model (Tomiyama, 1998) is a modification of the Antal model (Antal et al., 1991) and is based on experimental results in pipe flow, in which the Tomiyama wall lubrication coefficient depends on the diameter of the bubble column. Frank et al. (2004; 2008) generalized the Tomiyama wall lubrication force (Tomiyama, 1998) by removing the dependency on pipe diameter, pointing out that the Antal wall force and the Tomiyama lift force can increase the gas volume fraction near the wall, however the Antal wall force is too weak to balance the Tomiyama lift force. Therefore, one of the objectives of this thesis was to test the accuracy and effect of different wall lubrication force models.

All bubble column simulations in this thesis were first experimentally studied by Hartevelde (2005), who studied both cylinder and pseudo-2D bubble columns. The author investigated the flow behaviors of these columns using particle image velocimetry (PIV) and particle tracking velocimetry (PTV) to measure the velocities of bubbles and liquid tracers, respectively. Single point glass fiber probes were applied to determine the air volume fraction. The 2D pseudo bubble column was a cuboid 0.243 m in width, 0.99 m in height, and 0.04 m in depth. The initial

water level was 0.7 m. The cylinder bubble column was 15 cm in diameter and 2 m in height, with the initial water level at a height of 1.3 m for superficial gas injection velocities in the range of 0.015 m/s to 0.049 m/s. Hartevelde used a water level of 1 m for higher injection velocities. The results of this study showed that homogeneous flow can only be observed using uniform aeration for both 2D pseudo and cylinder bubble column geometries, with which very high gas volume fractions can also be maintained. With a high gas volume fraction (55%), the up-flow was very weak in the center of the bubble column, and the down-flow was observed very close to the wall. In Hartevelde (2005), a stability analysis was also performed in the 3D cylinder bubble column with uniform aeration to determine flow regimes at various superficial gas velocities, such as homogeneous and transition flows. When the superficial gas velocity u_g was less than 0.05 m/s, which is a relatively low velocity, the large-scale structures near the gas inlets depended on the aeration injection pattern. For the non-uniform air injection case, the effect of the large dynamic structure got weak at a higher location on the column compared with the uniform air injection condition. Near the gas injection region, the large dynamic structure happens due to instability.

Many CFD studies have been performed based on the experiments described in Hartevelde (2005). For example, Yuan et al. (2014) simulated Hartevelde's bubble column using the Euler-Euler model and quadrature-based method of moments, and found that the results of their simulations were in fairly good agreement with the experiments. The authors found that a homogeneous flow formed under uniform aeration, but the vortices in the simulations provided a larger non-aerated region compared to Hartevelde's experiments. This difference is probably due to a lack of front and back wall effects in the 2D simulations, because Hartevelde's (2005) pseudo

2D bubble column is actually a 3D rectangular bubble column and therefore contains front and back wall effects.

Another CFD study based on Harteveld (2005) was accomplished by Monahan and Fox (2009) that featured a complete study of sub-models for the two-fluid model, including the rotation and strain forces. The simulation results demonstrated reasonable agreement with the experimental results for uniform gas injection, but for other non-uniform injection patterns the simulation disagreed with the experiments.

Some of the studies using the two-fluid model to simulate bubble columns do not contain many of the sub-models mentioned previously. For example, the two-fluid model used by Pfleger et al. (1999) to simulate bubble columns only includes the drag force acting on bubbles and an additional source term for the continuity equation, which is turbulent dispersion. With turbulent effects, turbulent fluctuations can be created by bubble diffusion. Pfleger studied a laboratory-scale rectangular bubble column (20 cm in width, 45 cm in height, and 5 cm in depth) for experimental measurements using laser doppler anemometry (LDA), PIV, and PTV. The corresponding CFD simulations were performed based on these tests. The results of the CFD simulations and experiments showed good agreement when the grid size was fine enough and a turbulence model was also considered.

A similar study by Law et al. (2008) helped validate the Euler-Euler model for low and high gas injection velocities using 2D simulations that were then compared with experimental measurements by Rampure et al. (2003) and Mudde et al. (1997). Law et al. (2008) considered two interfacial sub-models, including drag and virtual mass, for simulating the 2D bubble column. Two drag coefficients were tested in Law study (Law et al., 2008) which include the Schiller and Naumann drag model (Schiller and Naumann, 1935) and the White drag model (White,

1974). The bubble pressure model was also added for the hydrodynamic interactions in the bubbly flow, which can affect the stability of the bubble (Spelt and Sangani, 1997). To maintain numerical stability, Law et al (2008) also applied bubble induce turbulence to their model (Sato et al., 1981). Ultimately, this study proved that the drag coefficient model depends on the vertical direction of the bubble column, therefore the Schiller and Naumann drag model performed better in the high vertical direction, while the White drag model performed better in the low vertical direction for time averaged profiles. Furthermore, the bubble dispersion model did not show a major effect at high superficial gas velocities.

1.4. Outline

Chapter 2 discusses the theory and governing equations of the two-fluid model, in addition to explaining the details of the sub-models used. Chapter 3 contains the results of the 2D and 3D CFD simulations of the pseudo 2D rectangular bubble column. Also, the simulated flow behavior was compared to the experimental data originally published in Hartevelde (2005). In Chapter 4, a mesh independent study and stability analysis of the simulated cylinder bubble column are completed, and compared the results obtained using the two-fluid model to Hartevelde (2005) again. Finally, Chapter 5 discusses the conclusion and future work of this project.

CHAPTER 2. THEORY AND EQUATIONS

2.1. Two-Fluid Model

Depending on the complexity level of the calculation, multiphase analysis can be accomplished using different methods. Researchers apply the two-fluid model for simulating bubble columns using the software OpenFOAM. Each phase, gas and liquid, is assumed to be an interpenetrating continuum and is identified by its volume fraction. The two-fluid model equations are governed by local instantaneous equations, which are used for ensemble averaging (Drew, 1982). The flow behavior for a gas-liquid flow can be described by continuity and momentum equations, and then solved using the two-fluid model.

The continuity equation describes the internal change of mass and mass flux in and out from the control volume, which is also called the conservation of mass.

$$\frac{\partial}{\partial t}(\rho_{\varphi}\alpha_{\varphi}) + \nabla \cdot (\alpha_{\varphi}\rho_{\varphi}\bar{U}_{\varphi}) = 0 \quad (1)$$

The left hand side of Eq. (1) describes the rate of change of mass and the convective flux passing the control volume, where ρ , α , and \bar{U} represent density, the volume fraction, and the velocity of the phase (φ), respectively. In a bubble column, we must consider two phases, with g and l standing for gas and liquid phases, respectively. The following relationship must be satisfied for the phase volume fractions.

$$\alpha_g + \alpha_l = 1 \quad (2)$$

The Naiver-Stokes equation, expanded by phase volume fraction, describes the conservation of momentum.

$$\frac{\partial}{\partial t}(\alpha_{\varphi}\rho_{\varphi}\bar{U}_{\varphi}) + \nabla \cdot (\alpha_{\varphi}\rho_{\varphi}\bar{U}_{\varphi}\bar{U}_{\varphi}) = \nabla \cdot (\alpha_{\varphi}\tau_{\varphi}) - \alpha_{\varphi}\nabla p + \alpha_{\varphi}\rho_{\varphi}\bar{g} + \bar{M}_{lb} \quad (3)$$

The right-hand side of Eq. (3) describes forces that are acting on phase φ inside the control volume, including viscous stress, pressure gradient, gravitational force, and $\bar{\mathbf{M}}_{lb}$ momentum exchange between the gas and liquid phases. τ_φ is the stress tensor, which is given by

$$\tau_\varphi = \alpha_\varphi \mu_\varphi \left[\left(\nabla \bar{\mathbf{U}}_\varphi + \nabla \bar{\mathbf{U}}_\varphi^T \right) - \frac{2}{3} (\nabla \cdot \bar{\mathbf{U}}_\varphi) \mathbf{I} \right] \quad (4)$$

in which μ_φ is the laminar viscosity, and \mathbf{I} is the unit tensor.

The momentum exchange term, $\bar{\mathbf{M}}_{lb}$, has a strong effect on the accuracy of the simulation prediction and the physical flow stability in the two-fluid model, which also contains the drag force, $\bar{\mathbf{M}}_d$, lift force, $\bar{\mathbf{M}}_l$, wall lubrication force, $\bar{\mathbf{M}}_{WL}$, virtual mass force, $\bar{\mathbf{M}}_{VM}$, turbulent dispersion, and heat transfer. All test cases in this thesis were laminar, hence, there was no turbulent dispersion to consider, and nor was there heat transfer between the liquid and gas phases. The simulations also did not include a bubble-induced turbulence model because the effect is very small. Therefore, this work considered only four forces, which are drag, lift, virtual mass, and wall lubrication, which are given in Eq. (5).

$$\bar{\mathbf{M}}_{lb} = \bar{\mathbf{M}}_d + \bar{\mathbf{M}}_l + \bar{\mathbf{M}}_{VM} + \bar{\mathbf{M}}_{WL} \quad (5)$$

For each force, different sub-models can be used for various cases, which are discussed in the following sections.

2.2. Drag Model

Drag is the most important force in bubbly flow, which has a strong effect on flow behavior, and it acts in the opposite direction relative to the bubble flow. The drag force of the bubbles in a bubble column depends on the drag coefficient, C_d , density of the liquid phase, ρ_l , relative velocity between gas and liquid, $\bar{U}_g - \bar{U}_l$, and the bubble diameter, d_g . Therefore, the drag force can be written as

$$\bar{M}_d = \frac{3}{4} C_d \rho_l \alpha_g \frac{|\bar{U}_g - \bar{U}_l|}{d_g} (\bar{U}_g - \bar{U}_l) \quad (6)$$

However, the drag coefficient depends on which drag model is used. Two drag models are tested in a pseudo-2D rectangular bubble column, including the Tomiyama drag law (Tomiyama et al., 1998) and the Tenneti drag law (Tenneti et al., 2011). The Tomiyama drag law strongly depends on the phase properties, such as density, gravity, and bubble diameter. The drag coefficient, C_d , can be written as

$$C_d = \text{Max}\left(\frac{24}{Re} (1 + 0.15 Re^{0.687}), \frac{8E_0}{3(E_0 + 4)}\right) \quad (7)$$

This drag law can be applied to distorted spherical bubbles, and the drag coefficient depends on Re and E_0 . Re is the bubble Reynolds number, which is defined as

$$Re = \frac{d_g |\bar{U}_g - \bar{U}_l|}{\nu_l} \quad (8)$$

in which d_g is the bubble diameter and ν_l is the liquid viscosity. E_0 in Eq. (7) is the Eötvös number and is defined as

$$E_0 = \frac{(\rho_l - \rho_g) g d_g^2}{\sigma_g} \quad (9)$$

in which g is the magnitude of the gravitational acceleration and σ_g is the surface tension. The Eötvös number describes the ratio of buoyancy force to the surface tension, which can describe the shape of the bubble in the liquid phase.

Another drag model tested is the Tenneti drag law (Tenneti et al., 2011), which is derived for gas-solid flow using practical-resolved direct numerical simulation. This improved drag correlation can be applied to the two-fluid model to predict the overflow behavior. The drag coefficient is calculated as

$$C_d = \frac{24}{Re} \alpha_l^2 \left(\frac{F_{isolated}}{\alpha_l^3} + F_0 + F_1 \right) \quad (10)$$

where α_l is the liquid volume fraction, and $F_{isolated}$ is the drag acting on an isolated surface of a sphere, derived from Schiller and Naumann's (1935) drag correlation.

$$F_{isolated} = \begin{cases} 1 + 0.15Re^{0.687} & Re \leq 1000 \\ \frac{0.44Re}{24} & Re > 1000 \end{cases} \quad (11)$$

F_0 and F_1 are given as

$$F_0 = \frac{5.81\alpha_g}{\alpha_l^3} + \frac{0.48\alpha_g^{\frac{1}{3}}}{\alpha_l^4} \quad (12)$$

$$F_1 = \alpha_g^3 Re \left(0.95 + \frac{0.61\alpha_g^3}{\alpha_l^2} \right) \quad (13)$$

2.3. Lift Model

The lift force is due to a bubble going through a fluid in a shearing motion, which forms a lift force perpendicular to the direction of the flow. This force pushes the bubbles to the center or wall of the bubble column. The lift force is given as

$$\mathbf{M}_l = C_l \alpha_g \rho_l (\bar{U}_g - \bar{U}_l) \times \nabla \times \bar{U}_l \quad (14)$$

and depends on the C_l lift coefficient and the vorticity of the continuous phase, which was a liquid phase in this thesis. Different lift models can affect the flow behavior, and in this work lift models were tested, including the Tomiyama (Tomiyama, 1998), Legendre and Magnaudet (Legendre and Magnaudet, 1998), Moraga (Moraga et al., 1999), and constant coefficient (Drew and Lahey, 1987) lift models.

The Tomiyama lift model applies to large deformable bubbles. The lift coefficient, C_l , highly depends on the bubble size and the Eötvös number, E_0 (Tomiyama et al., 1998). Therefore, the surface tension between the gas and liquid phases is very important. The lift coefficient in the Tomiyama lift model (Tomiyama, 1998) is given as

$$C_l = \begin{cases} \min[0.288 \tanh(0.121Re), f] & \text{for } E_{0d} < 4 \\ f & \text{for } 4 \leq E_{0d} \leq 10.7 \\ -0.27 & \text{for } E_{0d} > 10.7 \end{cases} \quad (15)$$

$$f = 0.00105 E_{0d}^3 - 0.0159 E_{0d}^2 - 0.0204 E_{0d} + 0.474 \quad (16)$$

This lift coefficient depends on the range of E_{0d} , which is a modified Eötvös number, defined as

$$E_{0d} = \frac{(\rho_l - \rho_g)gd_h^2}{\sigma_g} \quad (17)$$

where d_h is the maximum horizontal dimension of a bubble, based on the bubble diameter, d_g , and the Eötvös number as shown in Eq. (18).

$$d_h = d_g(1 + 0.163E_0^{0.757})^{\frac{1}{3}} \quad (18)$$

According to the Tomiyama lift model, large bubbles move toward the center of the bubble column because of the lift force.

The Legendre and Magnaudet (1998) lift model is more applicable to small spherical particles. Thus, this lift model can only be applied to non-distorted bubbles. The Legendre and Magnaudet model describes the lift force as depending on the Reynolds number and the shear rate, Sr , for $0.1 \leq Re \leq 500$ and $0 \leq Sr \leq 1$. The lift coefficient, C_l , of the Legendre and Magnaudet model is given as

$$C_l = \sqrt{C_{l_{low}}^2 + C_{l_{high}}^2} \quad (19)$$

where $C_{l_{low}}$ and $C_{l_{high}}$ are defined as

$$C_{l_{low}} = \frac{(6 \times 2.255)^2 Sr^2}{\pi^4 Re (Sr + 29)^3} \quad (20)$$

$$C_{l_{high}} = \left(\frac{0.5(Re + 16)}{Re + 29} \right)^2 \quad (21)$$

Sr is the dimensionless shear rate, shown in Eq. (20), which is the ratio between the difference of the liquid velocity across the bubble and the relative velocity of the gas and liquid, which is defined by Eq. (22).

$$Sr = \frac{d_g \nabla \bar{U}_l}{|\bar{U}_g - \bar{U}_l|} \quad (22)$$

For large Reynolds numbers ($Re \geq 300$) and moderate shear rates ($Sr \leq 0.2$), $C_l = 0.5$. It is known that when the Reynolds number is low, the lift coefficient strongly depends on the Reynolds number and shear rate. However, when the Reynolds number is high, those dependences become weak.

The third lift force model is the Moraga lift model (Moraga et al., 1999). This model is mainly used for solid spherical particles, but can also be applied to bubbles and liquid drops. The lift coefficient highly depends on the Reynolds number, Re , and the shear rate, Sr , which are described in the Legendre and Magnaudet lift model. The Moraga lift coefficient, C_l , can be defined by Eq. (23).

$$C_l = 0.2 e^{-Re \frac{Sr^2}{3.6 \times 10^5}} e^{-0.12 Re \frac{Sr^2}{3.0 \times 10^7}} \quad (23)$$

The last lift coefficient is the constant lift coefficient $C_l = 0.5$ (Drew and Lahey, 1987). This lift coefficient does not depend on any parameters, such as bubble shape, bubble diameter, or Reynolds number, etc.

2.4. Virtual Mass

Drag and lift are important forces in bubbly flow, but the acceleration of the bubbles in the liquid generates an additional force, which is called virtual mass or added mass force. This force is the inertia added to the system due to acceleration of the bubbles because the liquid surrounding the bubbles moves and accelerates with them. The virtual mass effect can be small compared with drag and lift forces. However, it can affect the numerical stability of the simulation (Paladino and Maliska, 2011). Virtual mass is defined as:

$$\mathbf{M}_{vm} = C_{vm} \alpha_g \rho_l \left(\frac{D\bar{U}_g}{Dt} - \frac{D\bar{U}_l}{Dt} \right) \quad (24)$$

in which D/Dt represents the material derivative, which describes the rate of change in the mass of the gas and liquid phases. C_{vm} is the virtual mass coefficient, which is a constant number. In this thesis, $C_{vm} = 0.5$ (Drew et al., 1979) for all simulations.

2.5. Wall Lubrication

In bubbly flow, when bubbles are close to the wall an extra force, called the wall lubrication force, prevents them from touching the wall due to the liquid flow between the wall and bubbles. Wall lubrication is described as:

$$\mathbf{M}_{wall\ lubrication} = -C_{WL} \alpha_g \rho_l |\bar{U}_l - \bar{U}_g|^2 \mathbf{n}_W \quad (25)$$

where C_{WL} is the wall lubrication coefficient, and \mathbf{n}_W is the unit normal vector pointing away from the wall.

Three wall lubrication models were tested in the 2D rectangular column simulations, including the Antal (Antal et al., 1991), Tomiyama (Tomiyama, 1998), and Frank (Frank et al., 2008) wall lubrication models. Antal et al. (1991) describe the wall lubrication coefficient as:

$$C_{WL} = \max \left\{ 0, \frac{C_{W1}}{d_p} + \frac{C_{W2}}{y_w} \right\} \quad (26)$$

where C_{W1} and C_{W2} are non-dimensional coefficients that are set as $C_{W1} = -0.01$ and $C_{W2} = 0.05$, d_p is the mean bubble diameter, and y_w is the nearest distance from the bubbles to the wall. Note that this wall lubrication model features a no-slip condition at the wall, which slows down the liquid velocity between the wall and the bubble in order for there to be an appropriate increase in the liquid velocity on the opposite side of the bubble.

The Tomiyama wall lubrication model (Tomiyama, 1998) is a modification of Antal's model and is based on experimental results in pipe flow. It is given as:

$$C_{WL} = C_W(E_0) \frac{d_p}{2} \left(\frac{1}{y_w^2} - \frac{1}{(D - y_w)^2} \right) \quad (27)$$

in which D is the diameter of the pipe. This model is limited by the bubble column geometry, but it can be more accurate than Antal's wall lubrication model when applied to pipe flows. The wall lubrication coefficient $C_W(E_0)$ highly depends on the Eötvös number, E_0 , which is related to the surface tension between the gas and the liquid:

$$C_W = \begin{cases} 0.47 & E_0 < 1 \\ e^{-0.933E_0+0.179} & 1 \leq E_0 \leq 5 \\ 0.00599E_0 - 0.0187 & 5 < E_0 \leq 33 \\ 0.179 & 33 < E_0 \end{cases} \quad (28)$$

The Frank wall lubrication model (Frank et al., 2004; Frank et al., 2008) was derived from the Tomiyama example (Tomiyama, 1998) by removing the model's dependence on col-

umn geometry. According to Frank et al. (2004; 2008), the wall lubrication coefficient, C_{WL} , is defined as:

$$C_{WL} = C_W(E_0) \max \left\{ 0, \frac{1}{C_{WD}} \cdot \frac{1 - \frac{y_w}{C_{WC} d_p}}{y_w \cdot \left(\frac{y_w}{C_{WC} d_p} \right)^{p-1}} \right\} \quad (29)$$

where C_W is determined by a function of the Eötvös number and is the same as in the Tomiyama model, as shown in Eq. (29). C_{WD} is the damping coefficient and determines the relative magnitude of the force. C_{WC} is the cut-off coefficient and determines the nearest wall distance relative to the bubble diameter where the force is active, and p is the power-law constant, which causes the force to fall off as a variable potential law described by: $M_{wall\ lubrication} \sim \frac{1}{y_w^p}$. In this work, these coefficients were set as $C_{WD} = 6.8$, $C_{WC} = 10$, and $p = 1.7$ (Frank et al., 2008).

2.6. Bubble Dispersion Force

The bubble dispersion force, or diffusive interfacial force, (Davidson, 1990) describes the hydrodynamic interaction between bubbles in a highly concentrated bubble column (i.e., high air volume fraction). This force can affect the physical stability due to the addition of the hydrodynamic effect. Bubble dispersion force is created by an uneven distribution of bubbles, which can also affect the liquid fluctuation. It can be difficult for a liquid to flow through a high gas concentration region. Instead, it will flow to a lower gas concentration due to the drag from the more concentrated area (Lee and Wiesler, 1987). Based on Davidson's (1990) expression of the diffusive interfacial force, the bubble dispersion force can be described as:

$$\mathbf{M}_{bubble\ dispersion} = -D\nabla\alpha_g \quad (30)$$

where D is the diffusivity term, which can be defined as:

$$D = \frac{3C_{ds}C_{dis}\rho_l(\bar{U}_l - \bar{U}_g)^2\sqrt{\alpha_g\alpha_l}}{4\alpha_l} \quad (31)$$

in which C_{ds} is the Tomiyama drag coefficient from the Tomiyama drag correlation (Tomiyama et al., 1998), and C_{dis} is the bubble dispersion coefficient, which in my simulations was set to a constant, $C_{dis} = 1$.

CHAPTER 3. PSEUDO 2D RECTANGULAR BUBBLE COLUMN

3.1. Experimental Overview

A 2D rectangular bubble column has been simulated to study the accuracy of the sub-models based on tests performed by Hartevelde (2005). In those experiments, the author investigated flow in a 2D bubble column using PIV and PTV to track the velocities of bubbles and liquid tracers, respectively. Hartevelde also used single point glass fiber probes to determine the air volume fraction within the column.

The bubble column was a cuboid shape 0.243 m in width, 0.99 m in height, and 0.04 m in depth. The initial water level was 0.7 m, as shown in Fig. 2(b). In this diagram, the blue-shaded area represents the liquid phase, and the red-shaded area represents the gas phase. The B1, B2, and B3 labels indicate the inlet, walls, and outlet, respectively. The walls were transparent, which allowed for observation and measurements. LDA was performed at the front wall of the reactor with the probe aligned in the vertical direction in order to measure mean liquid velocity. The top of the bubble column was open to air. Bubbles were injected through needles on the bottom of the bubble column with a superficial gas velocity of 0.02 m/s. The diameter of the bubbles ranged between 3.5 mm to 5 mm.

Hartevelde (2005) tested five injection patterns of aeration to investigate the flow behavior and to determine the homogeneity in the column as a function of different inlets. Fig. 2 (a) is the bottom view of the rectangular bubble column featuring different inlet patterns.

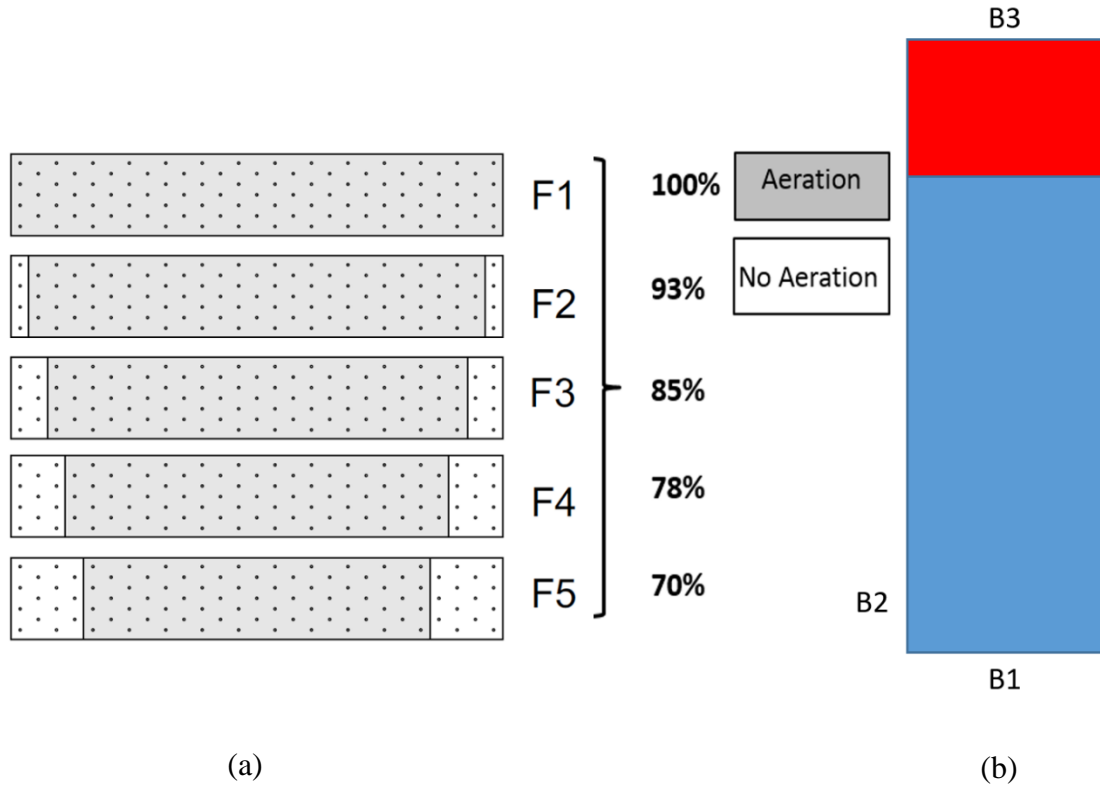


Fig. 2. (a) Aeration patterns for all 5 cases and (b) an schematic diagram of the 2D bubble column.

The shaded areas of Fig. 2 (a) indicate where gas injection occurs. Experimental results showed that homogeneous flow occurs for the uniform inlet geometry, which is case 1 (F1). Under these conditions, no large-scale structures were observed. For cases 2 (F2) and 3 (F3), which contain small non-aerated regions near the column wall, the author again observed no large-scale structures. However, for cases 4 (F4) and 5 (F5) in which the non-aerated area is up to 22% to 30% near the wall, large-scale dynamic structures started to appear (Harteveld, 2005).

3.2. Mesh Convergence Test

OpenFOAM was used to perform simulations of a 2D rectangular column based on the same dimensions from the experiments of Harteveld (2005), which were described in section 3.1

and Fig. 2. All five cases were used to validate the accuracy of the prediction of flow behaviors in the simulated bubble column. In Harteveld's experiments, the diameters of the bubbles were controlled between 3.5 mm to 5 mm. Therefore, a constant bubble diameter of 4 mm was applied for the CFD simulations. Also, the inlet superficial gas velocity was set to 0.02 m/s, which was the same as in the experiments.

Before testing different sub-models in OpenFOAM, a mesh convergence study needs to be completed. Three mesh sizes were tested, including 4 mm for a total of 14,700 cells ($60 \times 245 \times 1$), 2.5 mm for a total of 40,800 cells ($102 \times 400 \times 1$), and 1.5 mm for a total of 105,600 cells ($160 \times 660 \times 1$), which are shown in Table 1.

Table 1. Mesh convergence test for case 1.

	Mesh 1	Mesh 2	Mesh 3
Total Number of Cells	60×245×1	102×400×1	160×660×1
	(4 mm)	(2.5 mm)	(1.5 mm)

All three mesh cases featured the same bubble column geometries, phase properties, initial air velocity, sub-models, etc., and were solved using the two-fluid model in OpenFOAM. The only difference between these cases was the number of grid points in the simulation.

Boundary conditions for this test are shown in Table 2. B1 is the gas inlet, B2 is the left- and right-side walls, and B3 is the outlet of the bubble column, which is left open to atmosphere. The front and back wall effects were neglected since it was a 2D simulation. The gas and liquid phases contained in this simulation are air and water, respectively. The properties of these phase are shown in Table 3.

Table 2. Boundary conditions.

BC	Bubble Phase	Liquid Velocity	Liquid Pressure
B1 Inlet	Fixed Value	Fixed Value	Zero Gradient
B2 Wall	Zero Gradient	No Slip	Zero Gradient
B3 Outlet	Zero Gradient	Zero Gradient	Fixed Value

Table 3. Properties of the gas (air) and liquid (water) phases.

Properties	Value
Superficial Gas Velocity	0.02 m/s
Bubble Diameter	4 mm
Gas Density	1.2 kg/m ³
Liquid Density	1000 kg/m ³
Liquid Dynamic Viscosity	0.001 kg/(m s)

A uniform gas injection was used for the mesh convergence study. Fig. 3 shows the time-averaged air volume fractions at a height of $z = 0.7$ m from the bottom of the column for a total average of $t = 180$ s (total run time 200 s). The red circles in Fig. 3 correspond to the experimental results of Hartevelde (2005), and the lines represent the coarse, fine, and finer meshes. Results of all three grid sizes show good trends when compared to the experimental data, but they do not exactly match. There were no significant differences between the three mesh sizes, especially between the results of the 2.5 mm (102×400) and 1.5 mm (160×660) mesh sizes, which showed only a slight difference. Therefore, due to the calculation speed and efficiency, the 2.5 mm (102×400) grid size would be applied in further 2D rectangular bubble column tests.

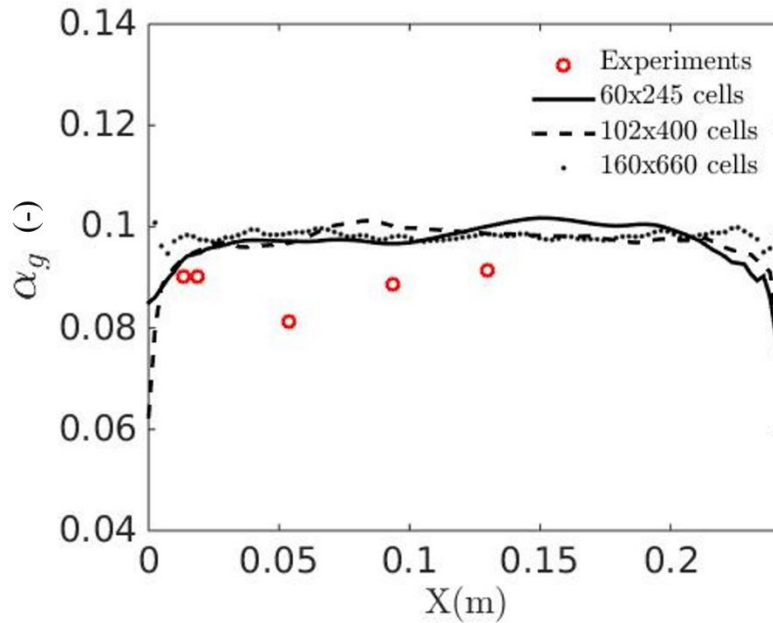


Fig. 3. 2D mesh convergence test at $z = 0.7$ m.

3.3. Sub-Model Accuracy Tests

3.3.1. Drag correlation tests

After determining the mesh size for simulations of the 2D rectangular bubble column, it was then necessary to test detailed sub-models (i.e., drag, lift, wall lubrication, and virtual mass force) for comparison with the experimental data described in Hartevelde (2005).

Two different drag models were tested first, since drag is the most important force in bubbly flow and has a strong effect in predicting flow behavior. The two drag models tested in this work included the Tomiyama (Tomiyama et al., 1998) and Tenneti drag laws (Tenneti et al., 2011), which were discussed in detail in Chapter 2.

The previously 2D rectangular bubble column geometry (section 3.1) was used to study these drag models, as well as the two-fluid model in OpenFOAM to solve the system. The Tomiyama lift model (Tomiyama, 1998), a constant virtual mass coefficient of $C_{vm} = 0.5$ (Drew and Lahey, 1987), and the Frank wall lubrication model (Frank et al., 2004) were also employed. Then compared the flow behaviors of the simulation using the Tomiyama and Tenniti drag correlations. The boundary conditions previously listed in Table 2 were applied here as well. Results were time averaged for $t = 180$ s for all cases.

For uniform air injection (case 1), the experimental results showed uniform air distribution and no large structures. The simulation results using both the Tomiyama and Tenneti drag laws showed a similar trend, but did not perfectly match the experimental data, as shown in Fig. 4. It was observed, however, that the Tomiyama drag law provided more symmetric bubble distribution near the inlet area than the Tenneti drag law. The global air volume fraction obtained using the Tomiyama drag law was also higher compared to the Tenneti drag law.

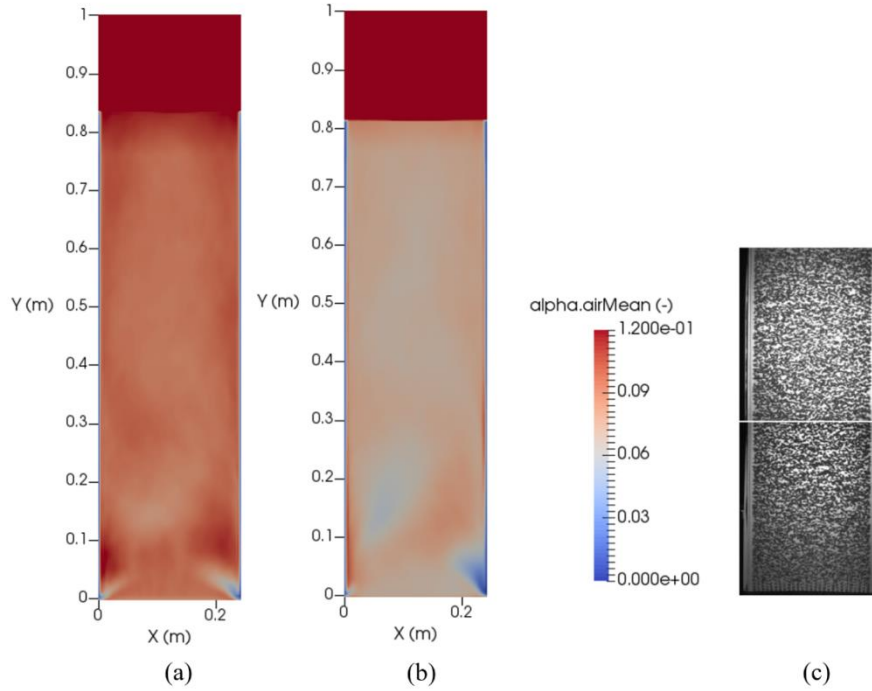


Fig. 4. Time averaged air volume fractions of case 1 using the (a) Tomiyama and (b) Tenneti drag correlations, and (c) the corresponding experimental result.

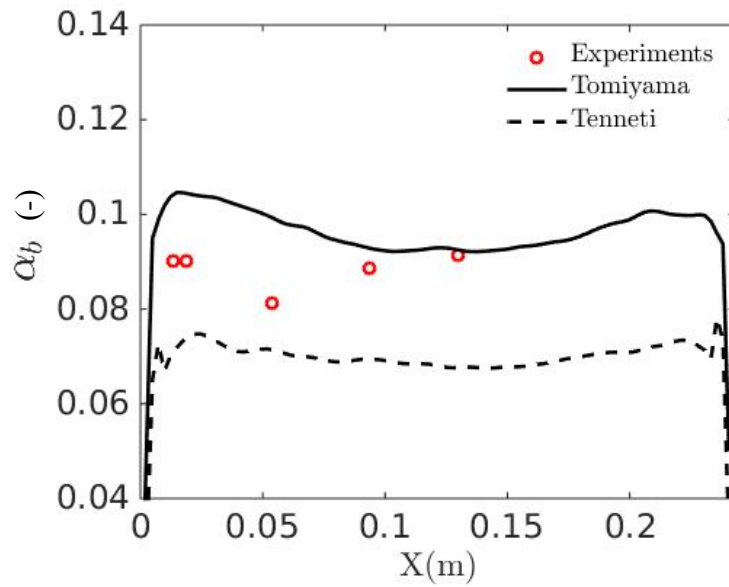


Fig. 5. Time averaged air volume fraction of case 1 at height $z = 0.7$ m

Fig. 5 compares these two drag laws with the experimental results for the time averaged air volume fraction at a height of $z = 0.7$ m. Results of both the Tomiyama and Tenneti drag laws showed a similar trend and close values to the experimental data. Thus, both drag correlations were in good agreement with the experimental results, but the simulated results using the Tomiyama drag law were closer to Hartevelde's (2005) work. The Tomiyama drag law provides a simulated time averaged air volume fraction of close to 10%, while the time averaged air volume fraction using the Tenneti drag law was around 7%.

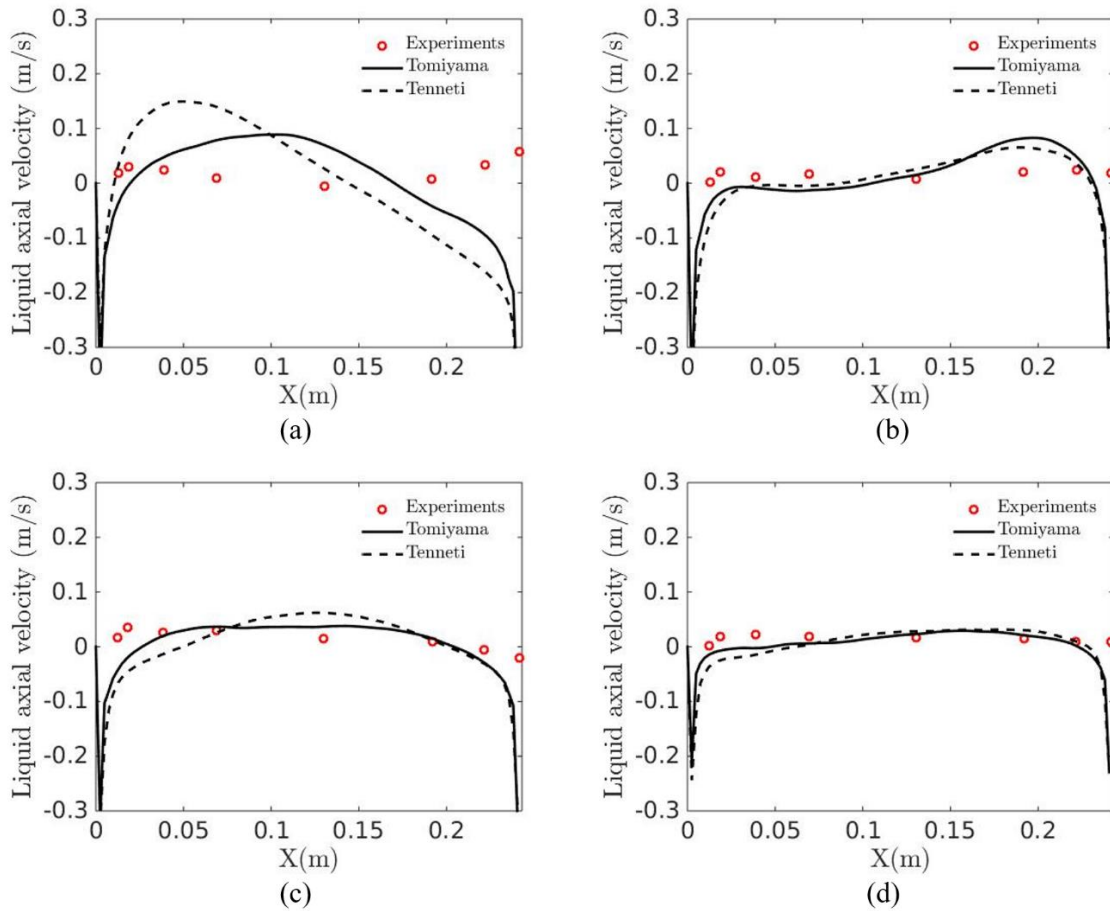


Fig. 6. Time averaged liquid axial velocity of case 1 at four different vertical locations in the bubble column, including (a) $z = 0.1$ m, (b) $z = 0.2$ m, (c) $z = 0.5$ m, and (d) $z = 0.7$ m. Simulated results were produced using the Tomiyama and Tenneti drag correlations.

To compare the profiles, such as void fraction and velocity, between the simulations and the experimental data, root mean square (RMS) values of the results were used, in which $RMS = \sqrt{\frac{1}{n} \sum_n x^2 [n]}$, where x represents the profile that is being compared ($x = \alpha_g$ or $x = u_g$). At $z = 0.7$ m, the RMS values of the Tomiyama and Tenneti results were $RMS (\alpha_g)_{Tomiyama} = 0.012$ and $RMS (\alpha_g)_{Tenneti} = 0.018$, respectively, which demonstrates that the Tomiyama drag correlation provides a better prediction compared to the Tenneti correlation. Fig. 6 shows the time averaged liquid axial velocity at four different vertical locations for case 1. Near the inlet area at $z = 0.1$ m, the differences between both the simulated results and the experimental data are significant, especially near the wall area, which is likely a result of the wall lubrication and lift model selections. When the locations get higher in the bubble column, both simulated results using the Tomiyama and Tenneti drag laws show better agreement with the experimental results, especially at $z = 0.7$ m. The RMS (u_g) values at each height are listed in Table 4, and from this information it is apparent that the Tomiyama drag correlation provides better simulated results.

Table 4. RMS values for the time averaged liquid axial velocities at different heights for the Tomiyama and Tenneti drag laws.

Height (m)	Tomiyama RMS (u_g) (-)	Tenneti RMS (u_g) (-)
$z = 0.1$	0.065	0.099
$z = 0.2$	0.037	0.042
$z = 0.5$	0.032	0.047
$z = 0.7$	0.018	0.027

Because the experimental results for the time averaged volume fractions and axial liquid velocities for cases 2–4 were missing, no detailed comparisons of the simulations and experiments are compared here. However, Fig. 7–9 compares the bubble distribution images of the simulations and experiments for cases 2–4. From the air distribution images in these three cases, both drag laws were in good agreement with the experimental images due to the similar gas distribution, especially for cases 3 and 4 near the inlet area. The figures show similar gaps between the inlet and walls since there was no air injected into the system near these regions. The gap size grows larger as the non-aerated area increases. Also, the time-averaged volume fraction of air becomes more symmetric as the aeration area decreases (Fig. 9). For these three cases, compared to the experimental results, the two-fluid model in OpenFOAM provides a good prediction for air distribution in the simulated bubble column.

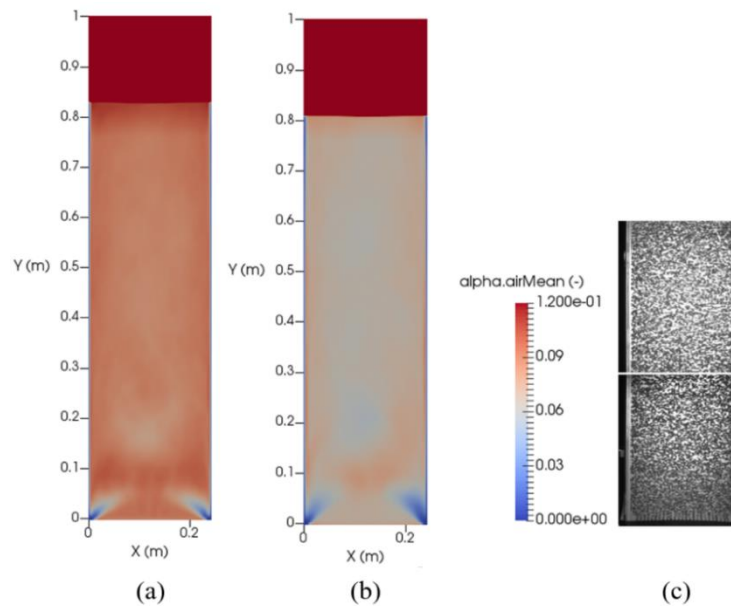


Fig. 7 The simulated time averaged air volume fraction of case 2 using the (a) Tomiyama and (b) Teneeti drag correlations. The corresponding experimental result is shown in (c).

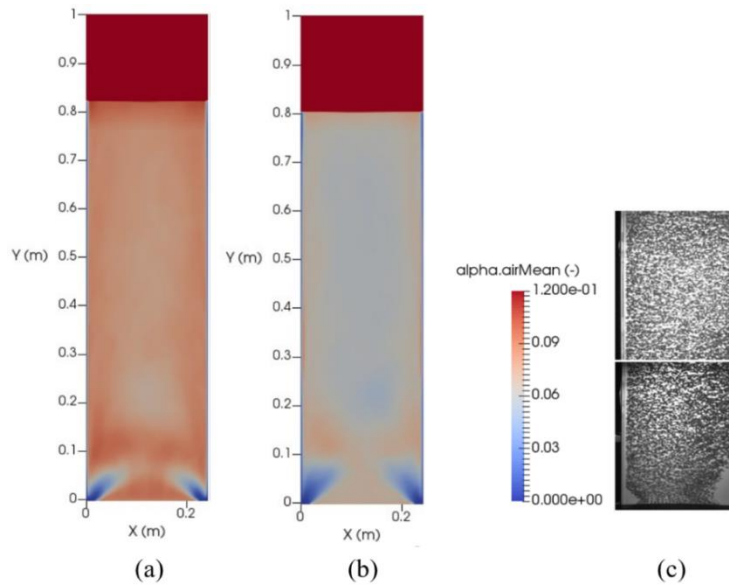


Fig. 8 The simulated time averaged air volume fraction of case 3 using the (a) Tomiyama and (b) Teneeti drag correlations. The corresponding experimental result is shown in (c).

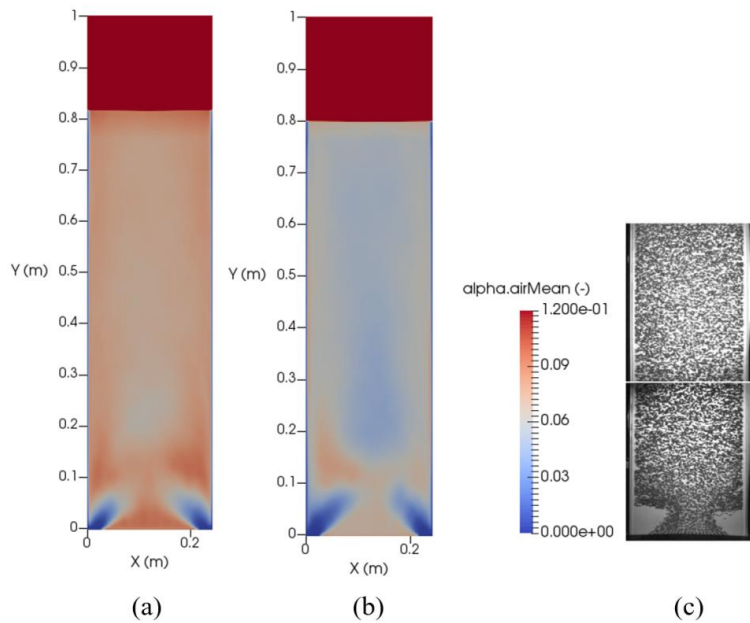


Fig. 9 The simulated time averaged air volume fraction of case 4 using the (a) Tomiyama and (b) Teneeti drag correlations. The corresponding experimental result is shown in (c).

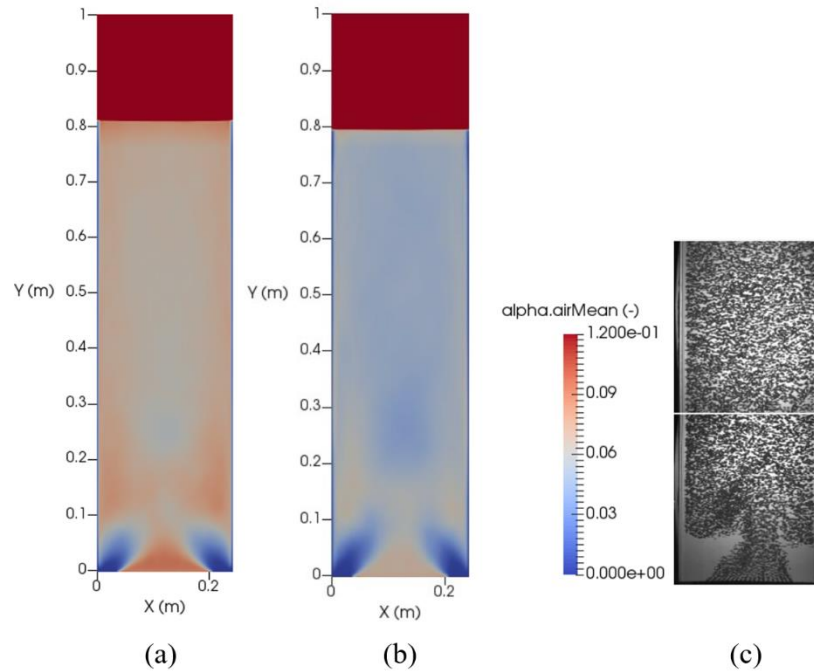


Fig. 10 The simulated time averaged air volume fraction of case 5 using the (a) Tomiyama and (b) Tenneti drag correlations. The corresponding experimental result is shown in (c).

For case 5, which has a 70% aeration area at the bottom of the column, the simulation provided a better symmetric profile of air distribution compared with all other cases for both the Tomiyama and Tenneti drag laws. The simulation profile is also closer to the experimental air distribution image shown in Fig. 10.

In Fig. 11, the air volume fraction in case 5 was high at the bottom center of the bubble column ($z = 0.05$ m). Simulation results using both the Tomiyama and Tenneti drag laws featured the same trend, but did not perfectly match the experimental results, which have a very low air volume fraction near the wall area and an almost 10% air volume fraction at the center of the bubble column. Simulation results obtained from both drag laws show that some air appears near the bottom wall area. The RMS values for simulation results using both drag laws and found that $\text{RMS}(\alpha_g)_{\text{Tomiyama}} = 0.035$ and $\text{RMS}(\alpha_g)_{\text{Tenneti}} = 0.026$, which means that the Tenneti drag correla-

tion gives a better prediction near the inlet area for less aeration at the bottom of the bubble column.

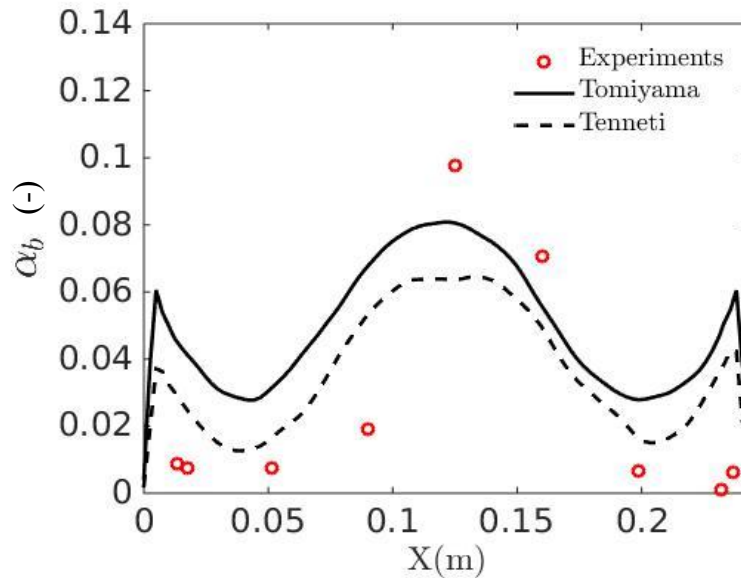


Fig. 11. The time averaged air volume fraction of case 5 at height $z = 0.05$ m; a comparison of the experimental and simulated data, using the Tomiyama and Tenneti drag laws.

At a higher position in the bubble column of $z = 0.7$ m (Fig. 12), the time-averaged air volume fractions obtained from both the Tomiyama and Tenneti drag laws are below the experimental results, however they follow the same trend. These results obviously show that the Tenneti drag law provides less agreement with the experimental results compared to the Tomiyama drag law, however, neither of the simulations followed the same trend as the experimental results, which have a center peak at this location. Moreover, near the wall area, the air volume fraction in the experiment is high, but the simulation results do not show this detail.

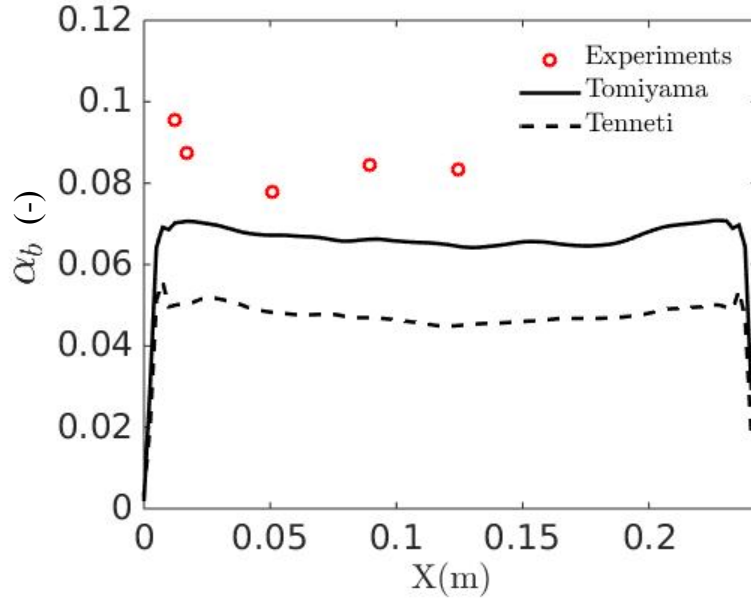


Fig. 12. The time averaged air volume fraction of case 5 at height $z = 0.7$ m; a comparison of the experimental and simulated data, using the Tomiyama and Tenneti drag laws.

The liquid axial velocities obtained from the Tomiyama and Tenneti drag laws are very similar (Fig. 13). At $z = 0.05$ m from the bottom of the column, the simulated liquid axial velocities show good agreement with experimental results. The RMS for each drag law were: $\text{RMS} (\alpha_g)_{\text{Tomiyama}} = 0.073$ and $\text{RMS} (\alpha_g)_{\text{Tenneti}} = 0.096$. Even better agreement with the experiments were obtained at a higher location in the bubble column ($z = 0.7$ m), particularly near the wall area ($\text{RMS} (\alpha_g)_{\text{Tomiyama}} = 0.042$, and $\text{RMS} (\alpha_g)_{\text{Tenneti}} = 0.058$).

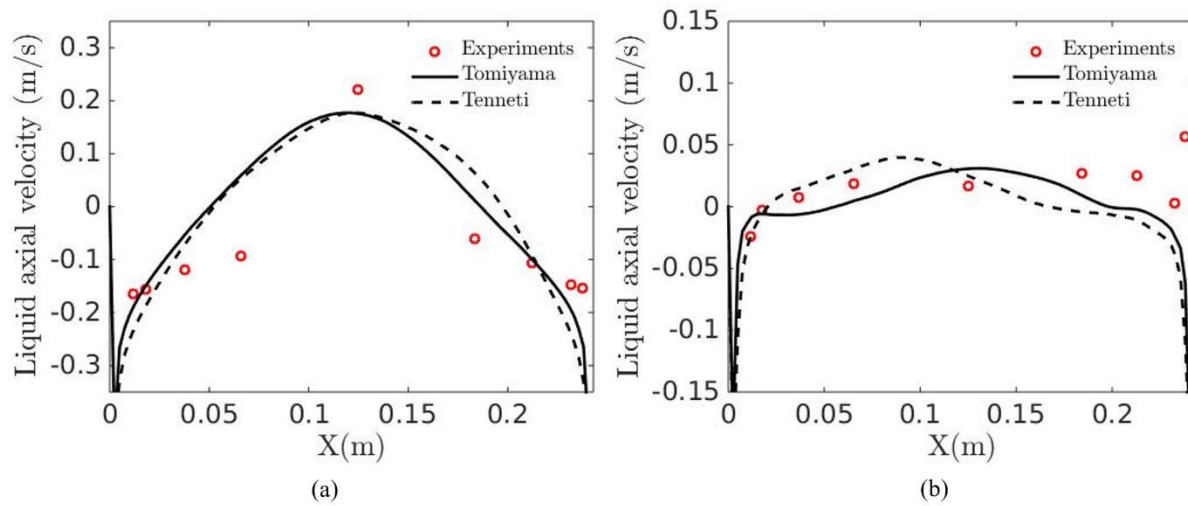


Fig. 13. Time averaged liquid axial velocity of case 5 at different vertical locations, including (a) $z = 0.05$ m and (b) $z = 0.7$ m, for both experimental and simulated results using the Tomiyama and Tenneti drag laws.

In summary, for all five cases, the air distribution profiles of the simulations were in good agreement with Harteveld's (2005) results, but do not perfectly match the experimental data, which is probably due to the effects of other interfacial force sub-models, such as lift, wall, and virtual mass forces. However, by looking at the Tomiyama and Tenneti drag law results overall, the simulations produced using the Tomiyama drag model were in better agreement with the experimental results when compared to the Tenneti drag law. This outcome is probably related to the fact that the cases studied are gas-liquid flows, while the Tenneti drag correlation was originally derived for gas-solid flows.

3.3.2. Lift force tests

Lift force is another important force that affects the flow behavior in bubbly flows. Lift force is caused by bubbles going through a fluid in a shearing motion. This force can push bub-

bles toward the center or walls of the bubble column, which can affect the air distribution in the reactor. Therefore, it is important to test the accuracy of different lift models. Four lift models were validated in this work, including Tomiyama's model (Tomiyama et al., 2002), the constant lift coefficient, Legendre and Magnaudet's model (Legendre and Magnaudet, 1998), and Moraga's model (Moraga et al., 1999). Detailed explanations of these models were discussed in Chapter 2.

The same 2D rectangular bubble column was been used to test the different lift models. The grid resolution, boundary conditions, and physical properties of the phases were the same as in the drag correlation tests. According to the results of the drag law tests, case 5 (70% aeration area at the bottom of the bubble column) resulted in larger differences between the simulation and experimental results, as compared with case 1 (100% aeration). Therefore, case 5 was used to validate the different lift models. Once again, the two-fluid model in OpenFOAM was used to solve the system, as well as various sub-models for the interfacial forces, including the Tomiyama drag model (Tomiyama et al., 1998), the constant virtual mass coefficient $C_{vm} = 0.5$ (Drew and Lahey, 1987), and the Frank wall lubrication model (Frank et al., 2004).

Fig. 14 provides the time averaged air volume fractions for different lift models. Simulation results of all models were in good agreement with the experimental image from Harteveld (2005). The differences between the time averaged air volume fractions for each model were not significant.

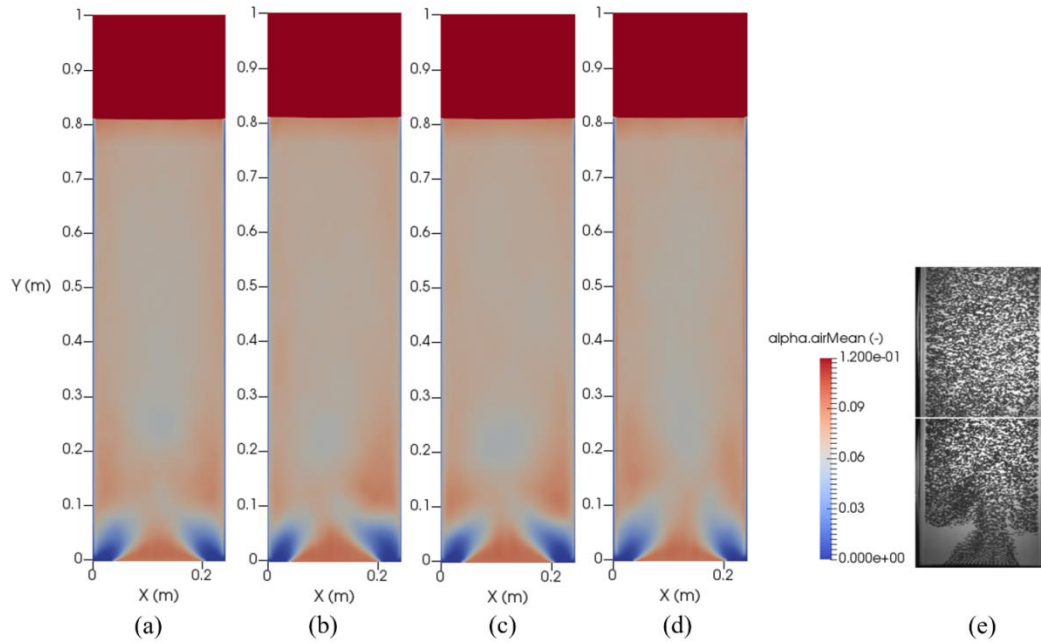


Fig. 14. The time averaged air volume fraction of case 5, featuring the (a) Tomiyama lift correlation, (b) constant coefficient lift correlation, (c) Legendre and Magnaudet lift correlation, and (d) Moraga lift correlation. The corresponding experimental result

Fig. 15 and Fig. 16 plot the time averaged air volume fraction at different locations of the bubble column. Near the inlet area, at a position of $z = 0.05$ m, all models trended with the experimental data. Table 5 shows the RMS (α_g) values for all lift models compared to the experimental results. Based on this table, we can see that both the Legendre and Magnaudet and constant coefficient lift models stand out, though the RMS values of all the lift models were very close to each other.

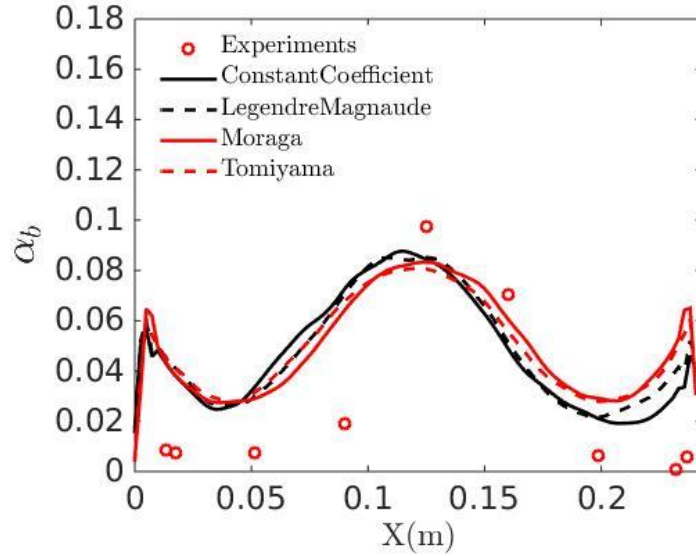


Fig. 15. The time averaged air volume fraction of the bubble column at height $z = 0.05$ m using different lift models.

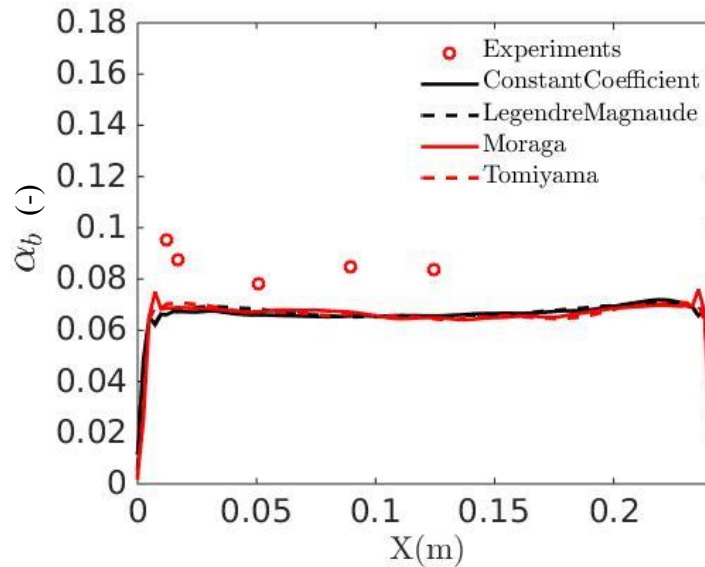


Fig. 16. The experimental and simulated time averaged air volume fraction results at a height of $z = 0.7$ m using different lift models.

Near the inlet area, at a location of $z = 0.05$ m, all the models provided fine agreement with the experimental data. Table 5 shows the RMS values for all lift models compared to the experimental results. Based on this table, the difference between each lift model is not significant

– the corresponding RMS (α_g) values were all very close to each other. However, the Legendre and Magnaudet and constant coefficient lift models provided a slight advantage in prediction compared to the other lift models.

Table 5. The RMS values for the time averaged volume fraction simulations at a height of $z = 0.05$ m using different lift models.

Lift Models	RMS (α_g) (-)
Tomiyama	0.035
Constant Coefficient	0.031
Legendre and Magnaudet	0.031
Moraga	0.036

At a location of $z = 0.7$ m, Fig. 16 shows that all lift models provide similar results, except the outcome of the Moraga lift model creates sharp peaks near the wall area. Table 6 shows the RMS values at this location, and the results indicate that the Tomiyama and Moraga lift models have small advantages compared with the other two lift models.

Table 6. The RMS values for the time averaged volume fraction results at a height of $z = 0.7$ m using different lift models.

Lift Models	RMS (α_g) (-)
Tomiyama	0.019
Constant Coefficient	0.021
Legendre and Magnaudet	0.020
Moraga	0.019

For the time averaged liquid axial velocities (Fig. 17) at $z = 0.05$ m, the profiles of the Tomiyama and Legendre and Magnaudet lift models were more symmetric, while the Moraga lift model provided better agreement at the center of column.

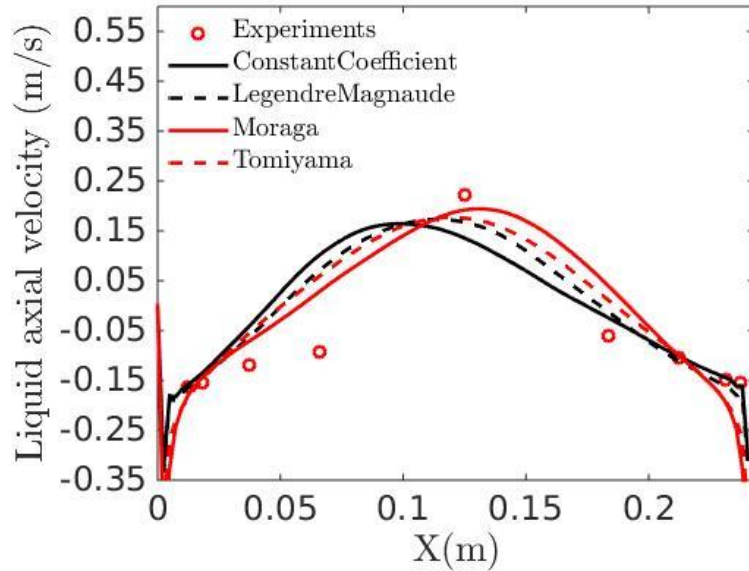


Fig. 17. The time averaged liquid axial velocity at $z = 0.05$ m for the experimental and simulated results using various lift models.

Table 7. The RMS values for the axial liquid velocity simulations at $z = 0.05$ m using different lift models.

Lift Models	RMS (u_g) (-)
Tomiyama	0.073
Constant Coefficient	0.077
Legendre and Magnaudet	0.063
Moraga	0.077

The RMS values for the time averaged liquid axial velocity at $z = 0.05$ m show that the Legendre and Magnaudet model stands out among those tested. There were no significant differences among the remaining three lift models.

Fig. 18 shows the time averaged liquid axial velocities at $z = 0.7$ m, in which the Moraga lift model appears to have better agreement with the experimental results among the models tested. However, when we look at the corresponding RMS values (Table 8), the Legendre and Magnaudet model stands out again, though not significantly.

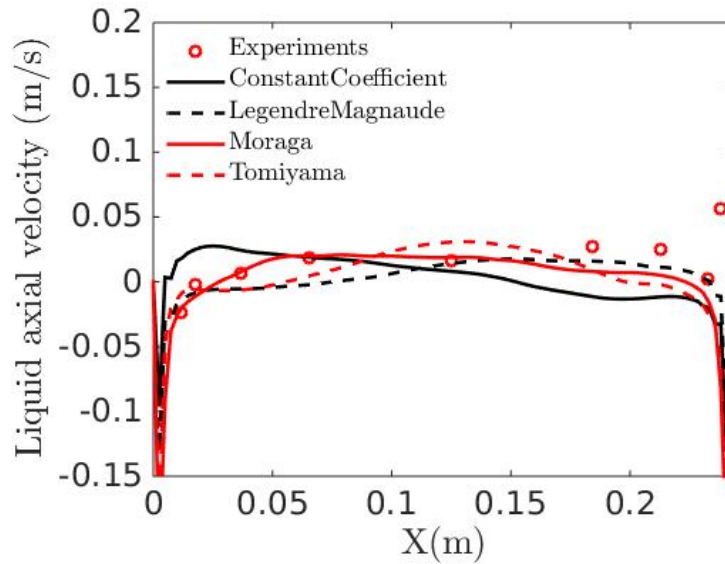


Fig. 18. The experimental and simulated time averaged liquid axial velocity at $z = 0.7$ m using different lift models.

Table 8. The RMS values for the axial liquid velocity simulations at $z = 0.7$ m using different lift models.

Lift Models	RMS (u_g) (-)
Tomiyama	0.042
Constant Coefficient	0.038
Legendre and Magnaudet	0.025
Moraga	0.046

In summary, there were no significant differences among the time averaged air volume fraction profiles of all four lift models studied, most likely due to the nature of the 2D case simulation, in which the influence of the lift force is not quite evident. The results of all the models show good agreement with the experimental results. However, the Legendre and Magnaudet lift model gives better agreements with the experiments for the time averaged axial liquid velocities. Therefore, Legendre and Magnaudet lift model was selected for further test simulations.

3.3.3. Wall lubrication force tests

The model for the wall lubrication force was the last sub-model been tested. Details of the wall lubrication force were discussed in Chapter 2. When bubbles are close to the column wall, an extra force acts on them. This force comes from the wall, and it prevents the bubbles from touching that boundary as a result of the liquid flow between the wall and the bubbles. Three wall lubrication models were validated in this work, including the Antal model (Antal et al., 1991), the Tomiyama model (Tomiyama, 1998), and the Frank model (Frank et al., 2004), which were explained in Chapter 2. In this simulation, the same 2D rectangular bubble column geometry was tested as in the previous section. The boundary conditions and physical properties of the phases were also the same and are listed in Table 2 and Table 3. Case 5, which has a 70% aeration area at the bottom of the bubble column, was the only case tested for the wall lubrication model studies. The two-fluid model in OpenFOAM was used to solve the system. Based on previous sub-model tests, The Tomiyama drag model (Tomiyama et al., 1998), a constant virtual mass coefficient $C_{vm} = 0.5$ (Drew et al., 1979), and the Legendre and Magnaudet lift model (Legendre and Magnaudet, 1998) were employed to describe the interfacial forces. Only the wall lubrication model was changed in each simulation to test the model's performance.

Fig. 19 is the time averaged air volume fraction at $t = 180$ s, in which the Antal, Tomiyama, and Frank wall lubrication models were tested and compared to the corresponding experimental bubble column image from Harteveld (2005). Differences among the results from these three models were not significant at the upper part of the column. However, near the inlet area (i.e., bottom of the column), the profile of the Antal wall lubrication model shows some differences from the profiles of the other two wall lubrication models, which is probably due to the fact that the Tomiyama wall lubrication model is modified from the Antal model based on experimental results. The profile of the Antal model is in good agreement with the experimental image in terms of bubble distribution and large scale structures near the bottom center of the inlet area.

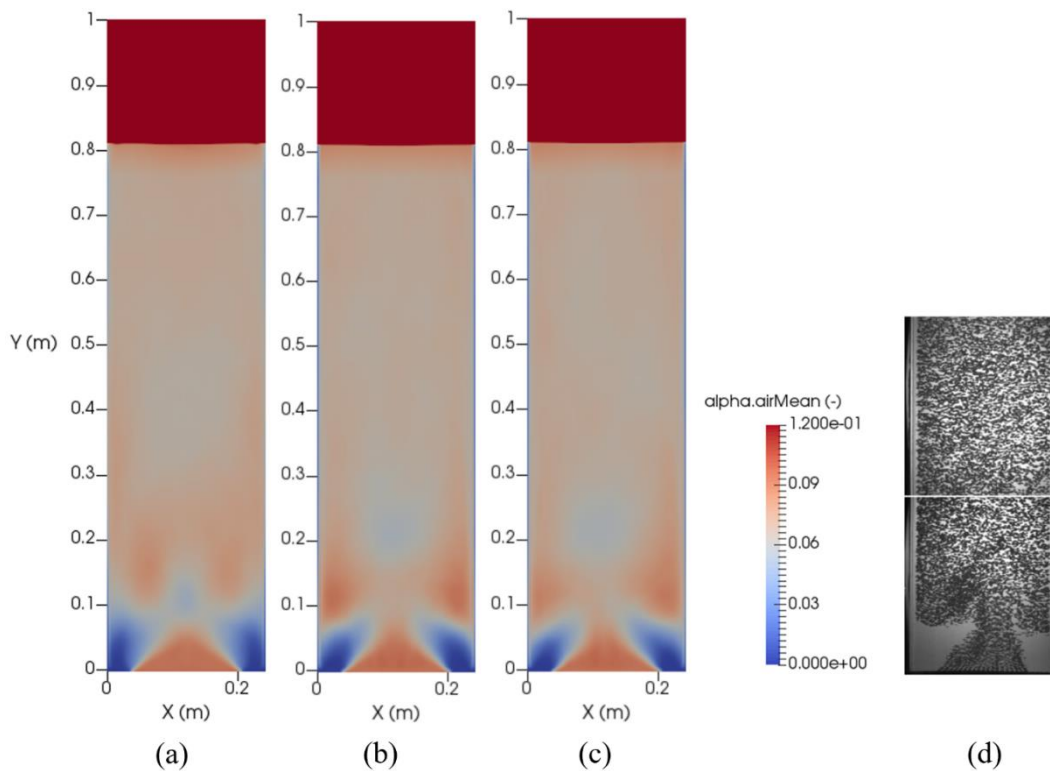


Fig. 19. The time averaged air volume fraction simulations of case 5 using the (a) Antal, (b) Tomiyama, and (c) Frank wall lubrication correlations. The corresponding experimental image is shown in (d).

There was no noticeable difference between the profiles of the Tomiyama and Frank wall lubrication models, which is consistent with the fact that the Frank wall lubrication model was derived from the Tomiyama model with the dependence of pipe diameter removed.

All three wall lubrication models provided symmetric profiles compared with experimental results (Fig. 20). Near the wall area, results of the Antal wall lubrication model were closer to the experimental data and featured less waviness compared with the results of the other two models. According to Table 9, the RMS (α_g) value of the Antal wall lubrication model was the smallest compared with the other two wall lubrication models. The RMS (α_g)_{Tomiyama} value was also very close to RMS (α_g)_{Frank} because the Frank wall lubrication model (Frank et al., 2004) was modified from the Tomiyama model. At a higher location, $z = 0.7$ m, the time averaged air volume fraction simulations for all three wall lubrication models were very similar to each other (Fig. 21), but overall smaller than the experimental results.

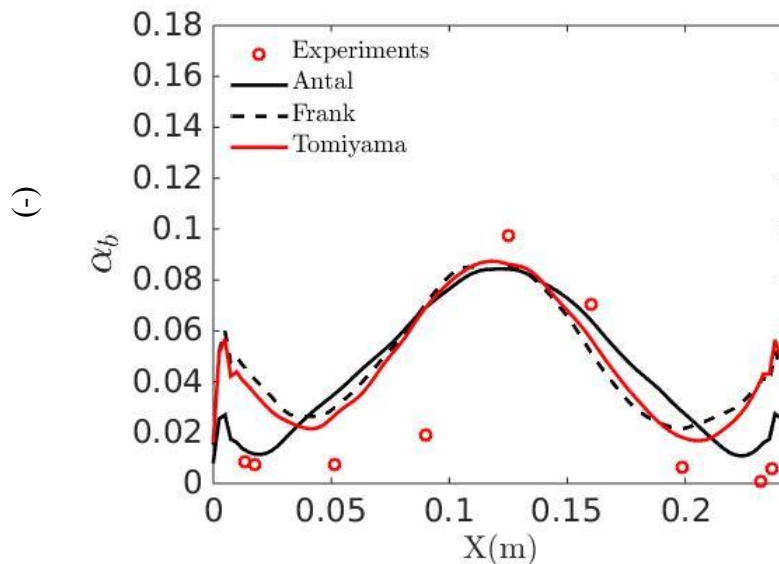


Fig. 20. The time averaged air volume fraction at $z = 0.05$ m for experimental and simulated results using different wall lubrication models.

Table 9. The RMS values for air volume fraction simulations at $z = 0.05$ m using different wall lubrication models.

Wall Lubrication Models	RMS (α_g) (-)
Antal	0.022
Tomiyama	0.033
Frank	0.031

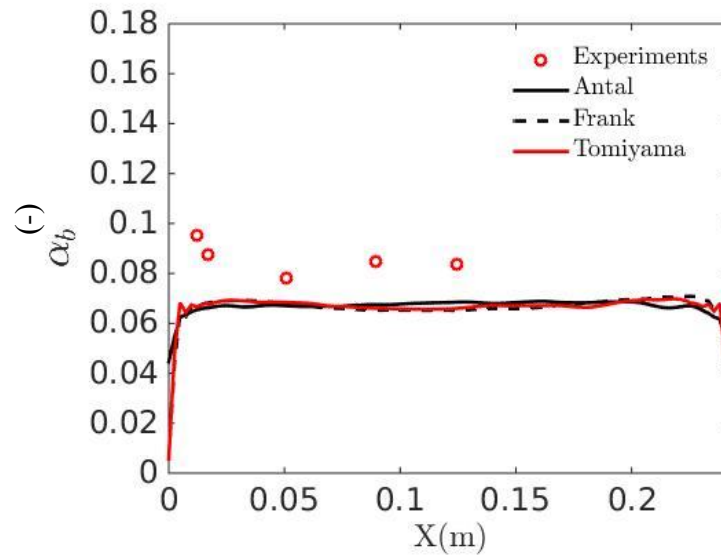


Fig. 21. The time averaged air volume fraction at $z = 0.7$ m for the experimental and simulated results using different wall lubrication models.

Table 10. The RMS values for the time averaged air volume fraction simulations at $z = 0.7$ m using different wall lubrication models.

Wall Lubrication Models	RMS (α_g) (-)
Antal	0.0199
Tomiyama	0.0198
Frank	0.0201

The RMS (α_g) values for these wall lubrication models were quite close (Table 10). Therefore, it seems these models do not affect air volume fraction so much at higher locations in the bubble column. However, for time averaged liquid axial velocities near the inlet area $z = 0.05$ m (Fig. 22), the Tomiyama and Frank wall lubrication models were in good agreement with the experimental results, while the simulation produced using the Antal wall lubrication model deviated from the results of the other two models and the experimental data (Table 11).

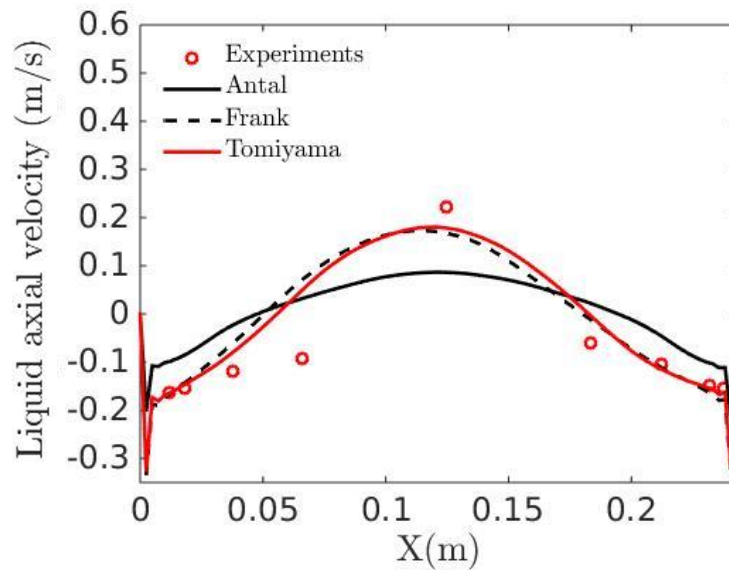


Fig. 22. The time averaged liquid axial velocity at $z = 0.05$ m for the experimental and simulated results using different wall lubrication models.

Table 11. The RMS values for the axial liquid velocity simulations at $z = 0.05$ m for different wall lubrication models.

Wall Lubrication Models	RMS (u_g) (-)
Antal	0.085
Tomiyama	0.055
Frank	0.063

At higher locations, $z = 0.7$ m, the result of the Antal wall lubrication model was better (Fig. 23) and was in good agreement with the experimental results. At this height, the overall differences among the results of these models became smaller (Table 12).

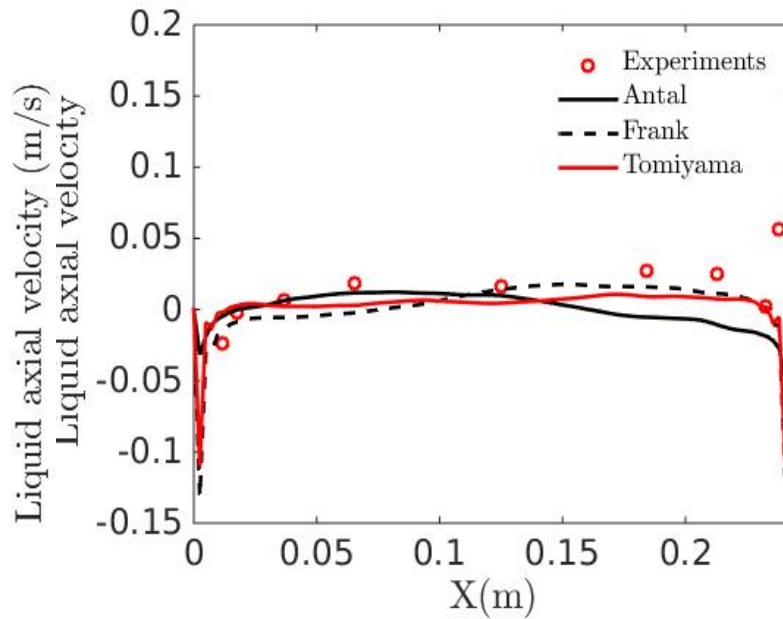


Fig. 23. The time averaged liquid axial velocity at $z = 0.7$ m for the experimental and simulated results using different wall lubrication models.

Table 12. The RMS values for the axial liquid velocity simulation at $z = 0.7$ m using different wall lubrication models.

Wall Lubrication Models	RMS (u_g) (-)
Antal	0.0300
Tomiyama	0.0250
Frank	0.0249

In summary, the results of all the wall lubrication models were in good agreement with the experimental results. For the time averaged air volume fraction simulations, the Antal model showed better agreement with the experimental data compared to the other two models, which may be due to the fact that the Tomiyama and Frank wall lubrication models are more applicable for pipe flows. However, for time averaged liquid axial velocity near the inlet location, the Antal model does not perform well, because the test cases were performed in a 2D geometry, which does not incorporate the wall lubrication forces from the front and back walls. Thus, the prediction may not perform accurately. Despite this shortcoming, the Antal wall lubrication model worked best overall was therefore applied to further test cases.

3.3.4 Conclusions and future work

The previous results indicate that for the laboratory-scale 2D rectangular bubble column, a 2.5 mm grid size can be used to develop simulations that show good agreement with the corresponding experimental results and without being very computationally expensive. For the selection of sub-models for future studies, The Tomiyama drag correlation selected for determining the further drag coefficient, since it trended well with the experimental results, as well as the

Legendre and Magnaudet and Antal models to simulate lift and wall lubrication forces, respectively. Constant virtual mass coefficient of $C_{vm} = 0.5$ applied for all simulations.

Overall, the simulation results of the selected sub-models showed good agreement with the experimental results, but still lacked accuracy. For example, at higher locations in the bubble column, the time averaged air volume fraction tended to be lower than the experimental data. This pattern is probably due to the fact that all the cases studied were 2D, which means the simulations do not consider effects from the front and back walls. For example, there is no liquid velocity in the front and back wall normal directions in the 2D case. However, wall forces also play a major role in predicting flow behavior. Therefore, in Section 3.5, 2D and 3D simulation results of the rectangular bubble column will be compared. In Hartevelde's (2005) experiments, the author calls the rectangular column a pseudo 2D column, but it is actually a true 3D bubble column. Therefore, 3D simulations need to be studied and compared with the experiments.

3.4. Stability Analysis in the 2D Rectangular Bubble Column

This section discusses the physical flow stability of the 2D rectangular bubble column. This study focuses on uniform air injection, which has 100% aeration at the bottom of the bubble column (case 1) since other patterns cannot create a uniform flow for stability analysis, particularly near the inlet area. "Stability" here refers not to numerical stability, but rather stability in terms of the observations of bubble structures. When air or bubbles are uniformly distributed in the bubble column, and no large dynamic structures are observed, we can define this condition as stable flow. Otherwise, when large dynamic structures appear, we define this bubble column condition as unstable. The objective of this study was to find out how initial conditions, such as inlet air velocity and inlet air volume fraction, influence the bubbly flow in the bubble column

reactor. To achieve this objective, first the instantaneous results and flow properties will be discussed. Then, compares how changes to the superficial gas velocity affect the column's flow behavior and properties, comparing the results with the first case.

3.4.1. Case review

In previous sections, the test of sub-models for different interfacial forces and ultimately selected the Tomiyama drag correlation (Tomiyama et al., 1998), the Legendre and Magnaudet (1998) lift model, and the Antal wall lubrication model (Antal et al., 1991) for the simulations in the rest of this work. In the previous studies, all simulation results were time averaged over $t = 180$ s. These averaged values are useful because they show the mean values of different parameters, such as air volume fraction and axial liquid velocity, in each cell. However, the instantaneous values at different times for each cell can be varied, and these instantaneous results allow us to perform a stability analysis on the bubble column simulation.

For uniform gas injection of the 2D rectangular bubble column, the superficial gas velocity was set to $U_{\text{air}} = 0.02$ m/s, which was the lowest superficial gas injection velocity reported in the Hartevelde (2005) experiments. The time averaged air volume fraction is shown in Fig. 24, in which the scale was set from 0 to 0.12. In this scenario, the air was well distributed in the water and we can observe no large-scale flow structures.

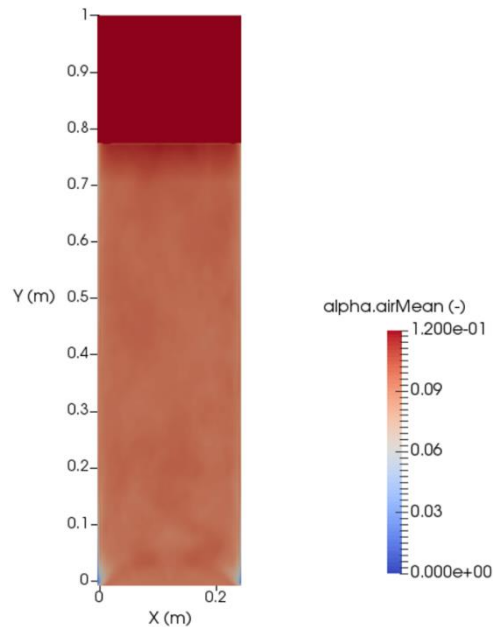


Fig. 24. The simulated time averaged air volume fraction of case 1.

However, for flow stability analysis, we need to establish an instantaneous air volume fraction. An example of an instantaneous air volume fraction of case 1 at $t = 20$ s is shown in Fig. 25, in which the same results are depicted at scale of 0–0.2 and 0–1. It is evident from these images that the 0–0.2 scale enables us to more easily observe flow behavior in the column. For example, at this scale, fluctuations close to the wall area can be observed, which have created some medium-scale structures and a region of low air volume fraction at the center of the bubble column. These fluctuations and disturbances are due to the lift and wall lubrication forces in combination with the boundary conditions, bearing in mind that this test case is 2D and therefore does not contain front or back wall effects.

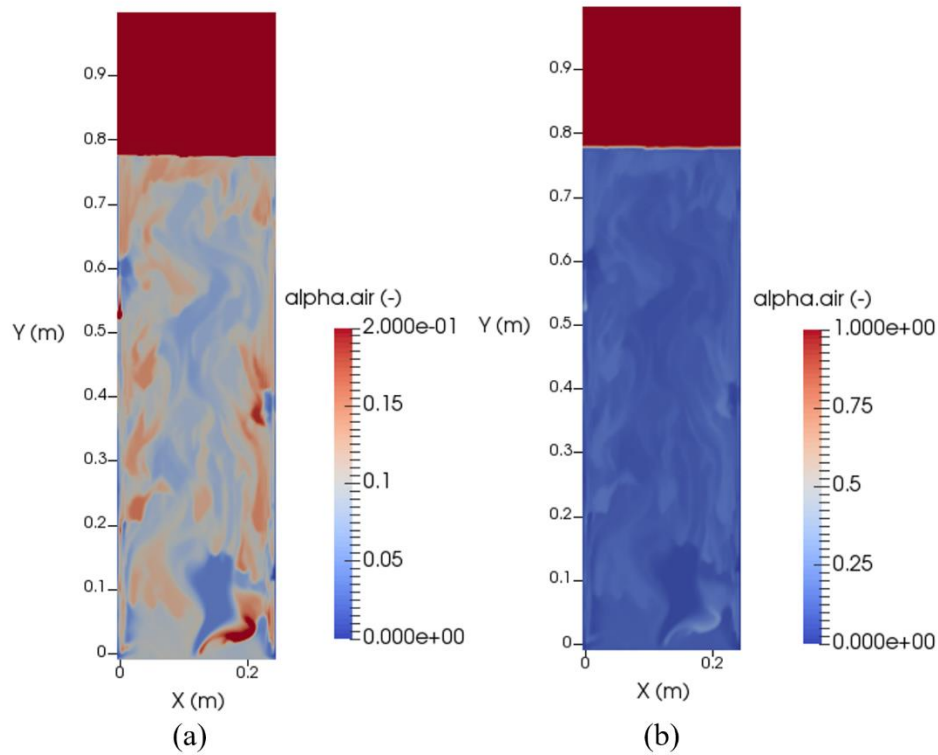


Fig. 25. The simulated air volume fraction of case 1 at $t = 20$ s at a scale of (a) 0–0.2 and (b) 0–1.

For $U_{\text{air}} = 0.02$ m/s, the flow shows some fluctuations, but not strong instability, where a large dynamic structure appears. To study the stability of the 2D rectangular bubble column, more simulations with higher superficial gas velocity were performed. Table 13 lists all the different superficial gas injection velocities, where $U_{\text{air} 1}$ is the original case 1. All cases were run for 20 s. The instantaneous air volume fractions at $t = 20$ s are shown in Fig. 26.

Table 13. Different superficial gas velocities.

$U_{\text{air}} 1$	0.02 m/s
$U_{\text{air}} 2$	0.04 m/s
$U_{\text{air}} 3$	0.06 m/s
$U_{\text{air}} 4$	0.08 m/s
$U_{\text{air}} 5$	0.10 m/s

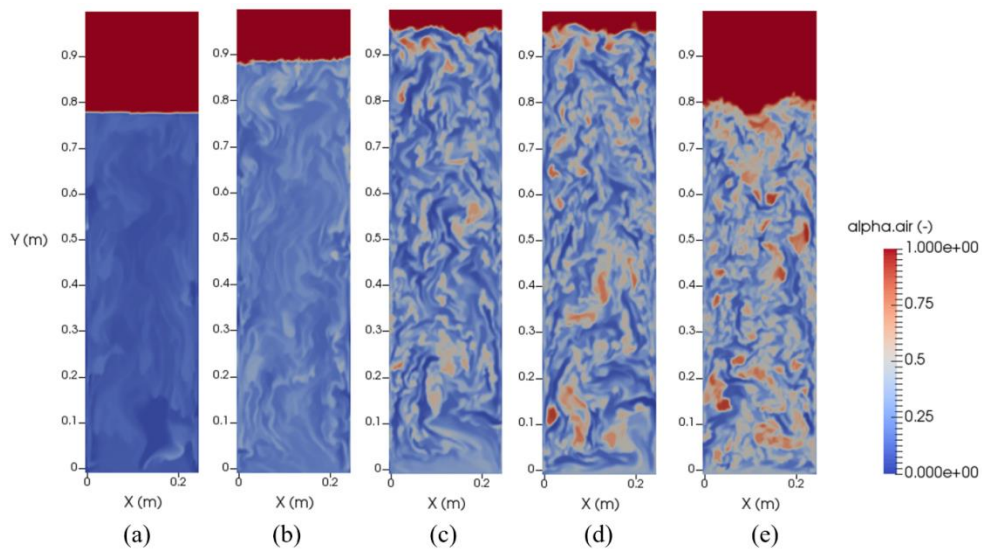


Fig. 26. The instantaneous air volume fraction simulations at different superficial gas injection velocities, including (a) 0.02 m/s, (b) 0.04 m/s, (c) 0.06 m/s, (d) 0.08 m/s, and (e) 0.10 m/s.

All these cases have the same boundary conditions and physical properties of the phases (see Table 2 and Table 3), except that the inlet superficial gas velocity is varied. However, the initial water level for the case with $U_{\text{air}} = 0.10$ m/s was set to 0.5 m instead of 0.7 m since water can escape the bubble column if the same initial water level is used, which can cause divergence in the simulation. With the same scale, the instability appears around the superficial gas velocity of $U_{\text{air}} = 0.04$ m/s, at which point a large dynamic structure began to appear. Then, more large-

scale structures show up and the formation of bubbles begin to form a cluster shape around $U_{\text{air}} = 0.06$ m/s.

In addition, the higher the superficial gas velocity, the earlier the large-scale structures appear. In Fig. 27 at $t = 1$ s, the first air injection velocity (0.02 m/s) maintains a uniform air distribution, but at higher superficial velocities the bubbles become unstable due to wall effects. For the last two air injection velocities, in which the superficial gas velocity becomes greater than 0.08 m/s, instability happens immediately, and large-scale structures are formed and exist until the end of the simulations.

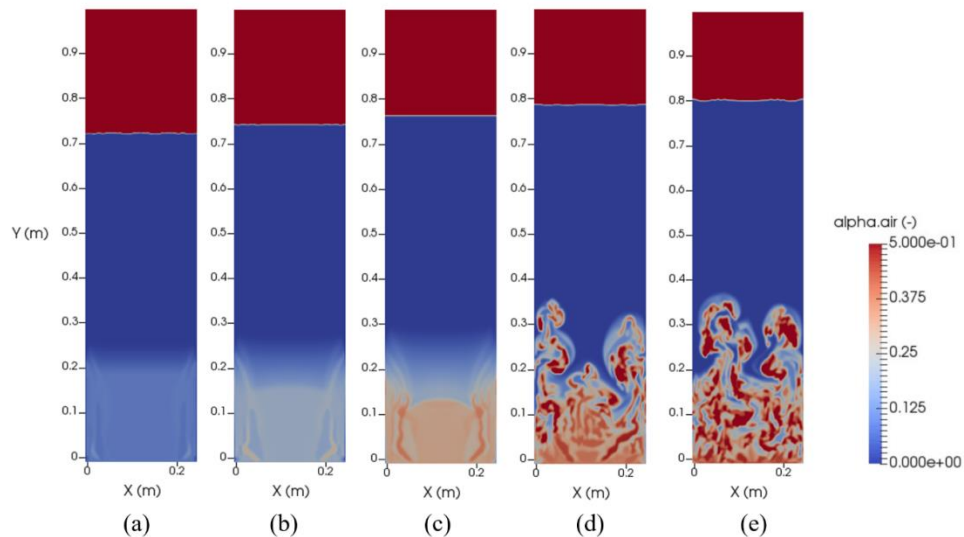


Fig. 27. The instantaneous air volume fraction simulations at $t = 1$ s for superficial gas velocities of (a) 0.02 m/s, (b) 0.04 m/s, (c) 0.06 m/s, (d) 0.08 m/s, and (3) 0.10 m/s.

3.4.2. Conclusions

There were no experimental results that could be used for comparison for the stability analysis of the 2D rectangular bubble column, and there are no published studies on stability analysis for simulations using the two-fluid model. In this analysis, the results show that instability happens beginning at a superficial gas velocity of $U_{\text{air}} = 0.02$ m/s, but was not very obvious.

When the superficial gas velocity increases to around 0.04 m/s to 0.06 m/s, bubble fluctuations become stronger and larger-scale structures start to appear. At an even higher superficial gas velocity, such as greater than 0.08 m/s, instability happens at the beginning of the simulation and continues to the end. Overall, for the 2D rectangular bubble column, results of the stability analysis are somewhat truncated due to the lack of experimental results with which to compare, and the fact that the front and back wall effects are not considered. Therefore, it is unable to determine a superficial gas velocity at which stable and uniform bubble distribution can be maintained. To study more information about this pseudo 2D rectangular bubble column, 3D simulations were studied and compared the results to experimental data.

3.5. Comparisons of 2D and 3D Simulations of the Rectangular Bubble Column

3.5.1. Case setup

After completing the 2D studies, 3D simulations of the bubble column were conducted based on the experimental work of Hartevelde (2005). The objective of this study was to use the sub-models validated in the previous sections and compare the 3D simulated results with experimental data. In general, 3D simulations tend to provide better results than 2D simulations when compared to experimental work. However, 2D simulations are generally less computationally expensive than 3D simulations and can provide relatively satisfactory predictions within a certain accuracy.

The same bubble column geometry being used as described in previous sections for the subsequent 3D tests. The initial water level was set to 0.7 m. The grid points in the height and width directions were the same as in sections 3.3 and 3.4. However, in the depth direction, ten grid points were used instead of one grid point as finished in the 2D simulations. The simulation

setup and physical properties of the phases were the same as in section 3.4. The boundary conditions are listed in Table 2, except that front and back wall effects were considered for the 3D simulations. The superficial gas injection velocity was $U_{\text{air}} = 0.02$ m/s for all cases in this section.

3.5.2. Comparison of 2D and 3D simulation results

Two cases were tested to compare the results with 2D simulations, including case 1 (100% aeration) and case 5 (70% aeration) (Fig. 28).

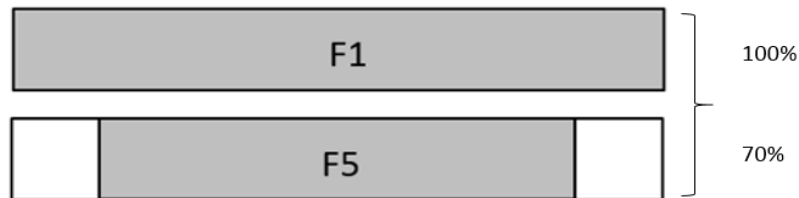


Fig. 28. The aeration patterns of the bubble column simulations for case 1 (top) and case 5 (bottom).

As described in previous sections, the two-fluid model was used to solve the system in conjunction with the Tomiyama drag model (Tomiyama et al., 1998), the Legendre and Magnaudet lift model (1998), the Antal wall lubrication model (Antal et al., 1991), and the constant virtual mass coefficient (Drew, 1979) to account for momentum exchanges between phases.

The simulations were performed for $t = 200$ s. Fig. 29 shows the time averaged air volume fraction of case 1. The first image (a) is the profile of the front wall. It indicates that in the vicinity of the wall the bubbles tend to concentrate near the inlet and outlet areas. The second image in Fig. 29 is the profile of the central slice of the 3D bubble column simulation, which shows that the air bubbles are well distributed in the middle of the column, and that the profile is similar to the 2D prediction. However the difference between the 3D and 2D time averaged air volume fraction profiles in Fig. 29 was not significant. Fig. 30 shows the time averaged air volume fraction at a height of $z = 0.7$ m from the bottom.

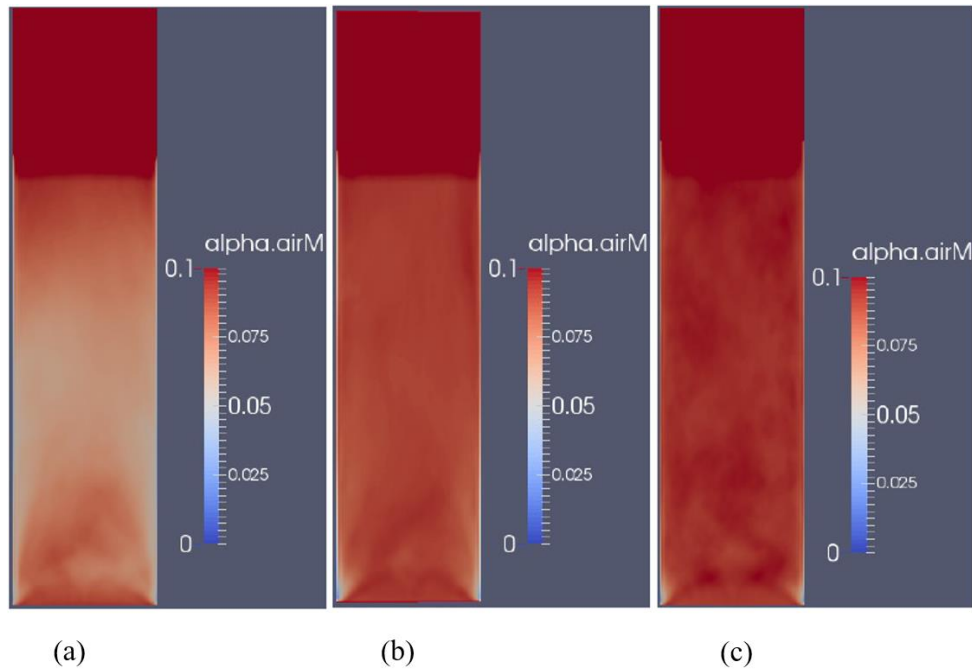


Fig. 29. A comparison of the time averaged air volume fraction simulations of case 1, including the (a) front wall and (b) central slice of the 3D simulation. The corresponding 2D case is shown in (c).

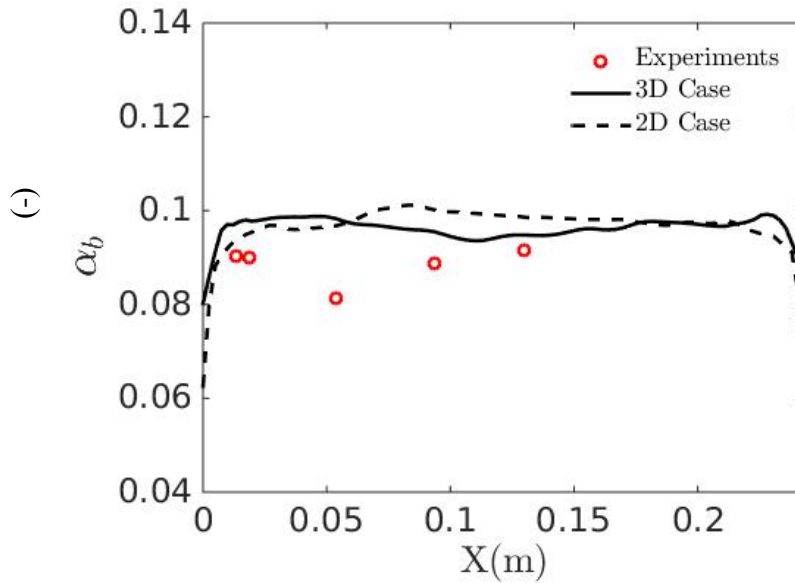


Fig. 30. Comparison of the time averaged air volume fractions at $z = 0.7$ m between the 2D and 3D simulations and experiments.

The RMS (α_g) values of the differences between the simulations and the experimental results are $\text{RMS}(\alpha_g)_{3D} = 0.009$ and $\text{RMS}(\alpha_g)_{2D} = 0.010$ for the 3D and 2D simulations, respectively, which indicates that the differences between the 3D and 2D simulation results were not significant.

Fig. 31 provides the time averaged liquid axial velocity of the bubble column at different heights. RMS values (Table 14) indicate the results of the 3D simulation were closer to the experimental results compared to the 2D simulation. Fig. 31 shows that the 3D simulation also has more symmetrical profiles than the 2D simulations. Near the inlet area, the liquid axial velocity of the 3D simulation was closer to experimental values. However, at higher regions (0.7 m), the differences between the 2D and 3D simulation results were very subtle.

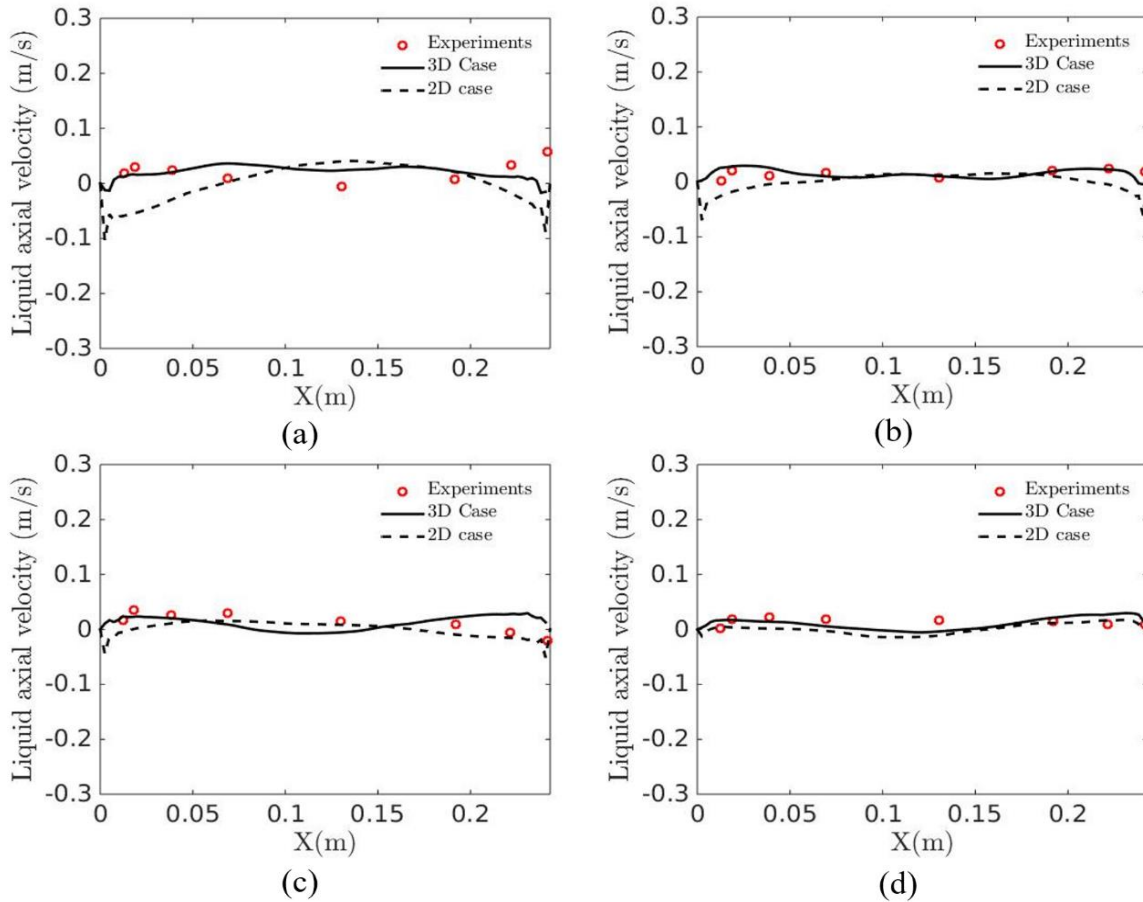


Fig. 31. Comparison of the time averaged liquid axial velocity for 2D and 3D simulations and experiments of the bubble column at different vertical locations, including (a) 0.1 m, (b) 0.2 m, (c) 0.5 m, and (d) 0.7 m.

Table 14. RMS values for the 2D and 3D axial liquid velocity simulations at different heights for case 1.

Vertical Location (m)	RMS (u_g) _{3D} (-)	RMS (u_g) _{2D} (-)
$z = 0.1$	0.028	0.060
$z = 0.2$	0.022	0.032
$z = 0.5$	0.022	0.023
$z = 0.7$	0.017	0.019

Next, the results of the 3D and 2D simulations were compared for case 5 (70% aeration). Fig. 32 is the time averaged air volume fractions of these simulations. The first image on the left is the profile of the front wall of the bubble column. The second image is the profile of the central slice. According to this simulation, the gas was pushed to the center of the column due to the wall effect. The profile of the central slice is similar to the experimental image shown in Fig. 10.

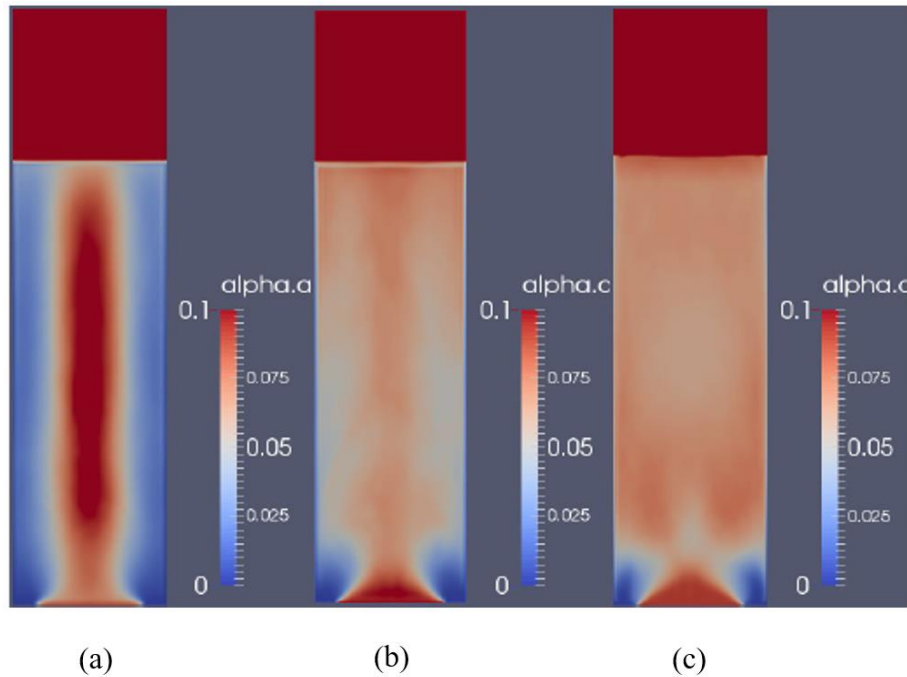


Fig. 32 Comparison of the time averaged air volume fractions for case 5, including the 3D (a) front wall and (b) central slice profiles. The corresponding 2D simulation is shown in (c).

Fig. 33 shows the time averaged air volume fraction at a height of $z = 0.05$ m from the bottom. The RMS values for the 3D and 2D simulations for this condition were $\text{RMS}(\alpha_g)_{3D} = 0.020$ and $\text{RMS}(\alpha_g)_{2D} = 0.023$, respectively, which means there was no significant difference between the two types of simulations for these conditions. However, near the wall area, the 3D simulation gave better results compared to the 2D simulation due to the presence of front and back wall effects. More time averaged air volume fractions at different heights are shown in Fig.

34. Compared with case 1 (100% aeration), the results of the 3D simulation do not agree with the experiment very well. Table 15 lists the RMS values for the time averaged air volume fraction simulations at different heights, which shows that the 2D simulation results agree with the experimental data better than the 3D simulation results at all heights except the highest location. However, the 3D simulation provides a good trend compared with the experimental results, especially at the higher regions of the bubble column, where the air volume fraction is high in the center of the bubble column. Overall, for the time averaged air volume fraction, the 3D simulation showed a good prediction compared with the experiment, but the results still lacked accuracy.

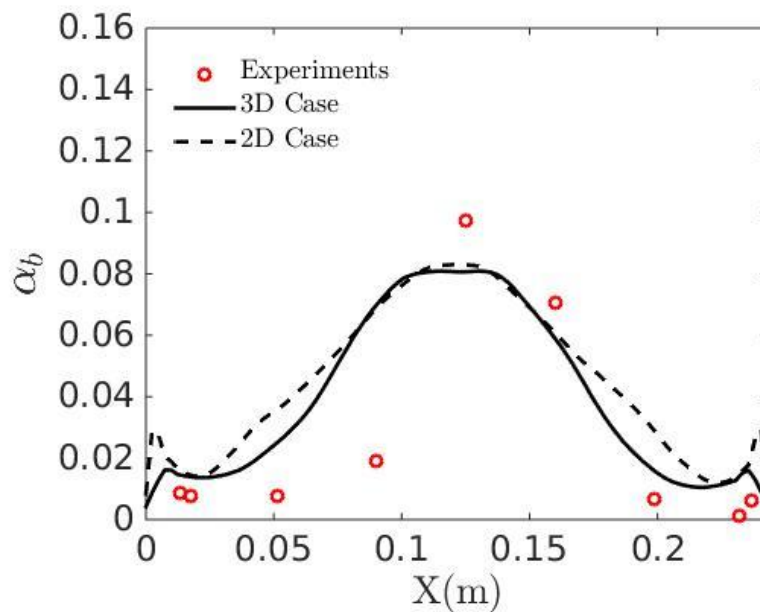


Fig. 33 Comparison of the time averaged air volume fractions of the 2D and 3D simulations and experiments at $z = 0.05$ m.

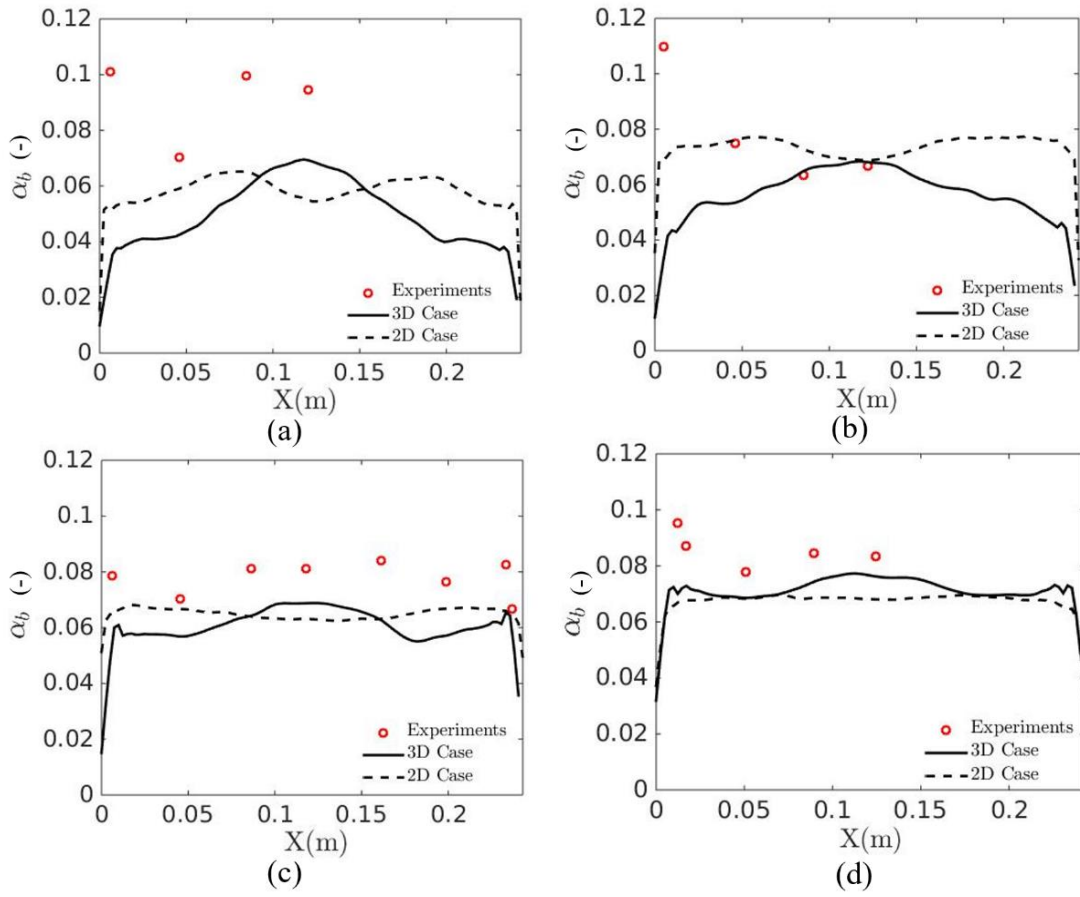


Fig. 34. Comparison of the time averaged air volume fraction 2D and 3D simulations and experiments of case 5 at different vertical locations, including (a) 0.1 m, (b) 0.2 m, (c) 0.5 m, and (d) 0.7 m.

Table 15. RMS values for the time averaged air volume fraction 2D and 3D simulations at different heights.

Vertical Location (m)	RMS (α_g)_{3D} (-)	RMS (α_g)_{2D} (-)
$z = 0.1$	0.028	0.060
$z = 0.2$	0.022	0.032
$z = 0.5$	0.022	0.023
$z = 0.7$	0.017	0.019

Next is the comparison of the time averaged liquid axial velocity with the experimental results. Fig. 35 shows the time averaged liquid axial velocity profiles at two different locations, including one close to the inlet and the other near the outlet area. Table 16 lists the RMS values of the differences between the simulation and experimental results. At a height of $z = 0.05$ m, the 3D simulation agreed well with the experiment in the center of the column. Near the wall the 3D simulation also provided a similar trend as the experimental data. At a height of $z = 0.7$ m, the 2D simulation results agreed better with the experimental data than the 3D simulation.

In summary, both 2D and 3D simulations provide good agreement with the experimental bubble column described in Hartevelde (2005). The 3D simulation showed more accuracy than the 2D simulation for the case with 100% aeration at the bottom of the column (case 1).

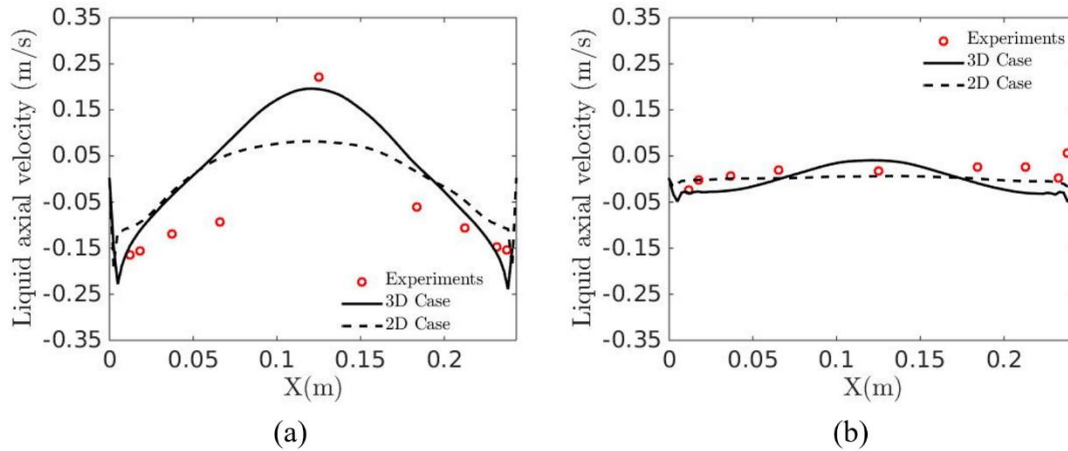


Fig. 35. Comparison of the time averaged liquid axial velocity of the 2D and 3D simulations and experiments for case 5 at two different vertical locations, including (a) 0.05 m and (b) 0.7 m.

Table 16. RMS values of time averaged liquid velocity 2D and 3D simulations at different heights.

Vertical Location (m)	RMS (u_g) _{3D} (-)	RMS (u_g) _{2D} (-)
$z = 0.05$	0.074	0.087
$z = 0.7$	0.040	0.029

3.5.3 Conclusions

For the laboratory-scale rectangular bubble column reactor, the two-fluid model in OpenFOAM provides good predictions using both 2D and 3D simulations. All simulations showed good flow behavior and air distribution, especially for case 1 (uniform air injection). 3D simulations can provide more accurate predictions than 2D simulations since 3D simulations also consider front and back wall effects. However, 3D simulations are often too expensive to perform.

Take this work for example: it took approximately four weeks to complete one 3D simulation. 2D simulations have less accuracy, but they can provide good trends and agreement with the experiments, and they are faster to run. For example, it took about five days to complete a 2D simulation in this work. Therefore, depending on the user's needs, such as time constraint and accuracy requirements, they may choose accordingly between 2D and 3D simulations of rectangular bubble columns.

For further investigation, more 3D simulations of a cylindrical bubble column were performed since this type of reactor geometry is widely used in industry. In the following chapter, more detail of the cylinder bubble column would be discussed in detail.

CHAPTER 4. CYLINDRICAL BUBBLE COLUMN

4.1. Experimental Overview

The cylindrical bubble column of Hartevelde (2005) is considered in this chapter to further investigate the predictive capabilities of the two-fluid model in OpenFOAM for bubbly flow applications. The bubble column under consideration has an inner diameter of 0.15 m and a total height of 2 m, as shown in Fig. 36 from Hartevelde (2005). At the bottom of the bubble column, there were 559 needles, each with an inner diameter of 0.8 mm for air injection. Depending on the flow rate of the injected air, the author changed the number of open needles. Hartevelde (2005) considered five different injection patterns, which are shown in Fig. 37. Table 17 provides the number of open needles for those aeration conditions. Pattern C1 was the case which was used in this work to perform a flow stability analysis for cylindrical bubble column simulation with different gas superficial velocities. In the experiments, the flow rate was controlled by 1 ml/s to 3 ml/s, and the bubble size distribution remained nearly uniform.

Table 17. Gas injection patterns for the cylinder bubble column.

Patterns	Needle Opening $\alpha < 15\%$	Needle Opening $\alpha > 15\%$	Aeration
C1	187	559	100%
C2	151	451	81%
C3	115	343	62%
C4	75	265	42%
C5	108	342	58%

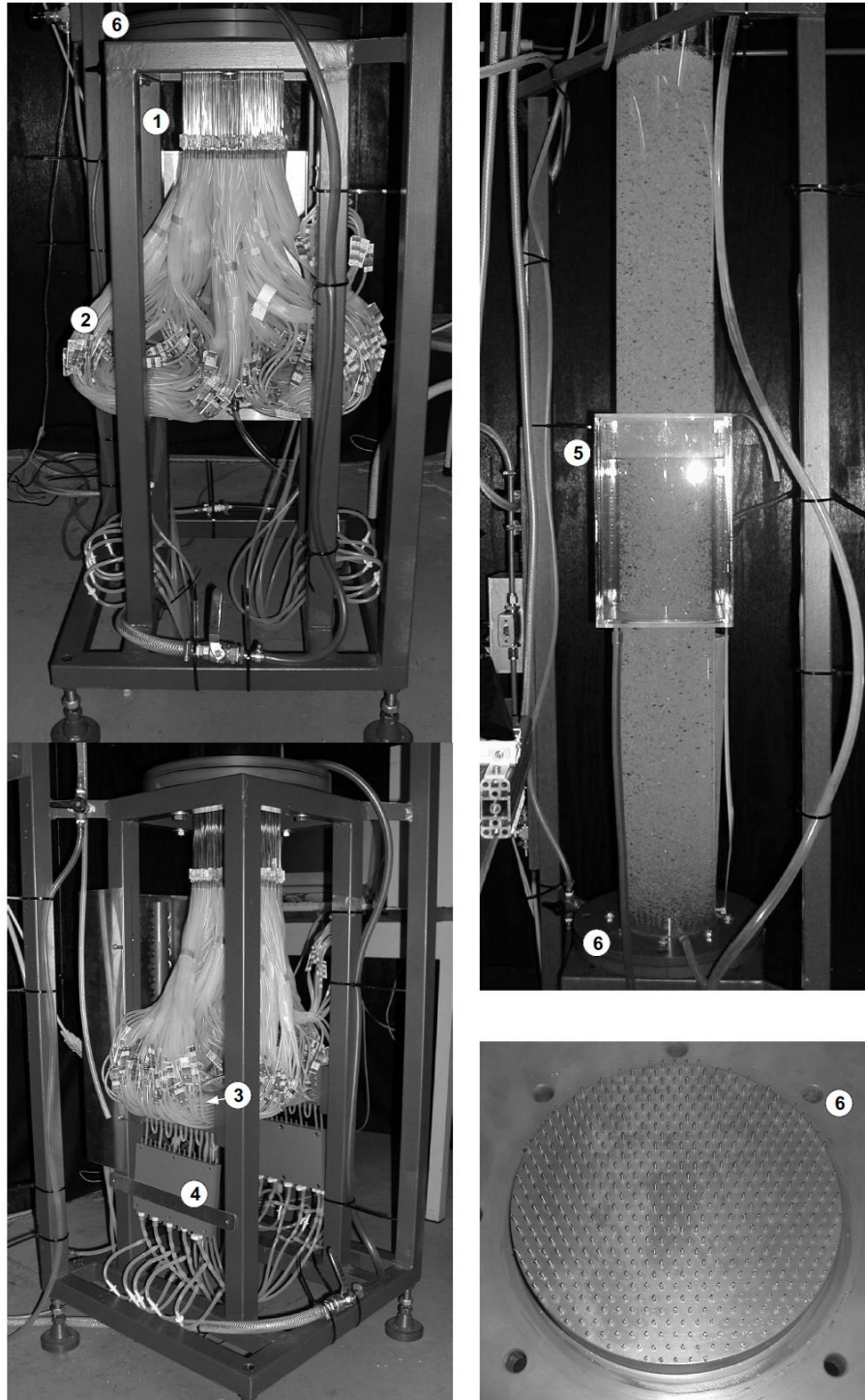


Fig. 36. The Harteveld (2005) experimental setup for the cylindrical bubble column. The different parts shown include: (1) needles; (2) hoses between needles and the group distributor; (3) group distributor; (4) group needles; (5) rectangular vessel (used for LDA); and (6) sparger.

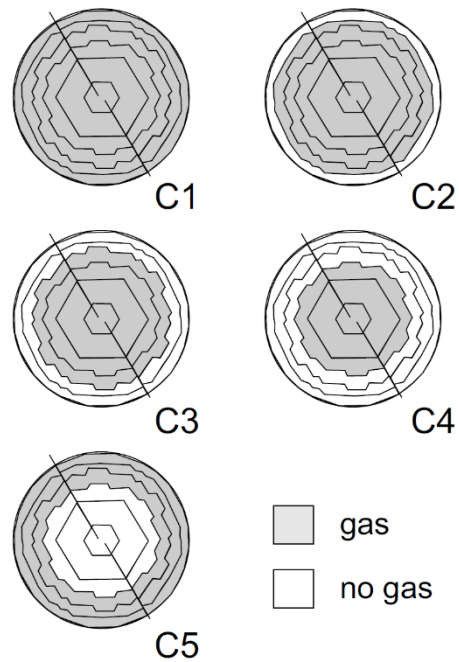


Fig. 37. The cylinder bubble column gas injection patterns by Harteveld (2005).

4.2. Mesh Convergence Test for the Cylindrical Bubble Column

Since the geometry of the rectangular bubble column considered in the previous sections is entirely different from the new system, it was necessary to perform a new stability analysis of the 3D cylinder bubble column. In order to do that, a mesh independence study also needed to be conducted to show the convergence of the numerical solution, the conditions of which may have changed due to differences in the flow conditions and mesh structure of the new bubble column geometry. In this section, The mesh convergence test would be discussed and compare the flow behavior of the system using two different mesh sizes.

The cylindrical bubble column in the OpenFOAM simulation discussed in this section has an initial water level of 1.3 m from the bottom of the bubble column. Two phases were contained in the column: gas (air) and liquid (water). The superficial gas velocity was $U_{\text{air}} =$

0.023 m/s. In the experiment, the bubble diameter was between 3 mm and 5 mm. Therefore, in the OpenFOAM simulation, bubble diameter was set as a fixed value of $d_{\text{air}} = 4$ mm.

Two meshes were tested for this geometry. One mesh has cells of 4 mm (402,320 total cells) and the other of 2 mm (1,050,000 total cells). Fig. 38 shows one example mesh of the column's bottom plane (left). A front view of the bubble column is shown on the right-hand side of the same figure, where the blue area corresponds to the water phase and the red area to the gas phase. The mesh shown is not uniform due to the circular shape of the simulated bubble column, therefore central cells are smaller than those near the wall. During the mesh generation, it ensured the maximum allowed cell dimension was used at the wall.

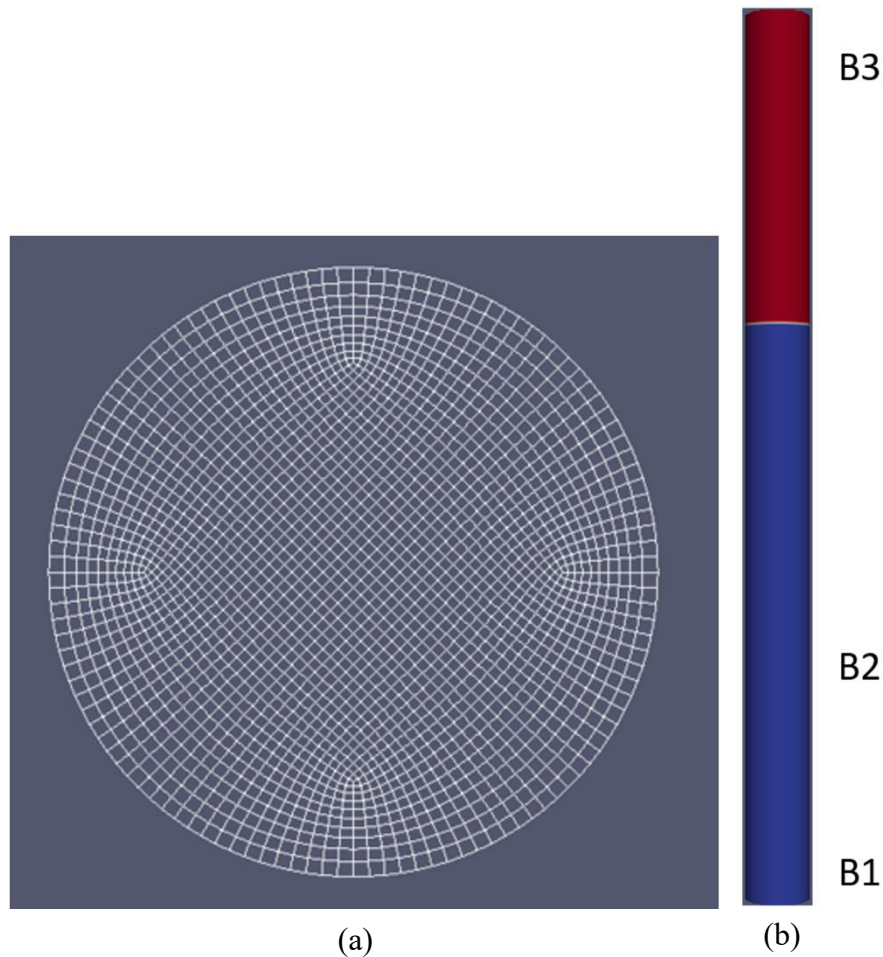


Fig. 38. (a) Mesh example of the bottom plane of the cylinder bubble column. (b) The OpenFOAM front view of the same system. The blue-shaded area is the liquid phase, and the red-shaded area is the gas phase.

As described in previous sections, the two-fluid model to model was used this system, with different sub-models for the interfacial forces, including the Tomiyama drag model (Tomiyama et al., 1998), the Legendre and Magnaudet lift model (1998), the Antal wall lubrication model (Antal et al., 1991), and a constant virtual mass coefficient (Drew et al., 1979), which were used to account for the momentum exchanges between phases. The boundary conditions for the simulation are shown in Table 18. B1 is the gas inlet. B2 is the wall of the bubble column, and B3 is the outlet, which is open to the atmosphere.

Table 18. Boundary conditions.

BC	Bubble Phase	Liquid Velocity	Liquid Pressure
B1 Inlet	Fixed Value	Fixed Value	Zero Gradient
B2 Wall	Zero Gradient	No Slip	Zero Gradient
B3 Outlet	Zero Gradient	Zero Gradient	Fixed Value

Results of the simulations were averaged starting from $t = 20$ s to avoid accounting for the initial phases of the simulation when the column was still filling with gas. Fig. 39 provides the time averaged air volume fraction results (from $t = 20$ s to 70 s) for the coarse and fine mesh simulations compared to the experimental results. Table 19 shows the RMS values of the two different volume fraction simulations using different mesh sizes compared again to the experimental data.

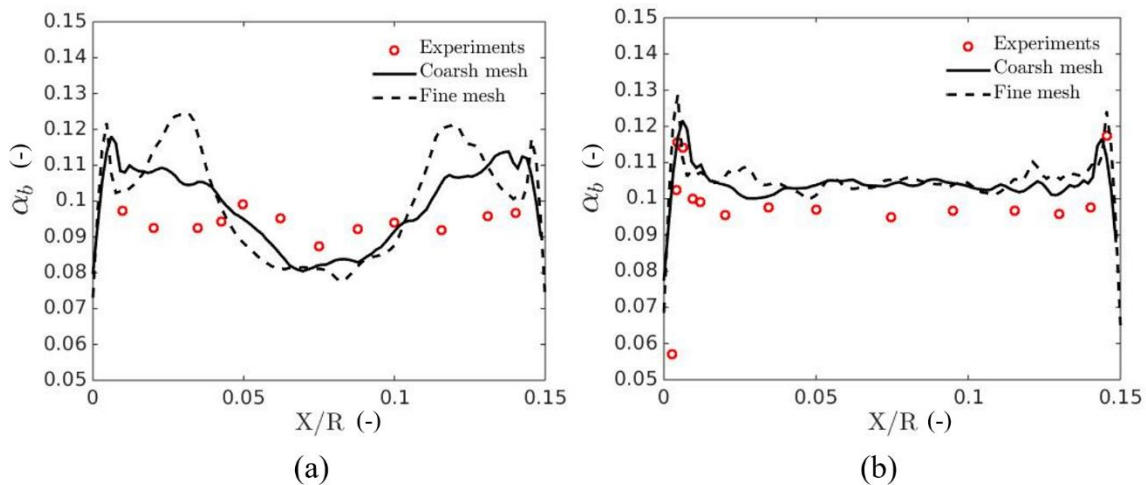


Fig. 39. Comparison of the time averaged air volume fraction simulations and experiments over $t = 50$ s at a height of (a) 0.07 m and (b) 0.15 m.

Table 19. The RMS values for the time averaged volume fraction simulations at different heights over $t = 50$ s.

Vertical Location (m)	RMS $(\alpha_g)_{\text{coarse}}$ (-)	RMS $(\alpha_g)_{\text{fine}}$ (-)
$z = 0.05$	0.011	0.015
$z = 0.7$	0.015	0.018

According to the RMS values, there was no significant difference between the two mesh sizes. The time-averaged volume fraction profiles obtained with the two meshes were in agreement with the experiments. However, the simulation with the coarsest mesh had a significantly lower time-step. Near the inlet area, at $z = 0.07$ m from the bottom, the difference between simulation and experimental results was more apparent than near the wall area. Also, there were some oscillations in the profiles, which considered a longer averaging time interval (20s – 90s).

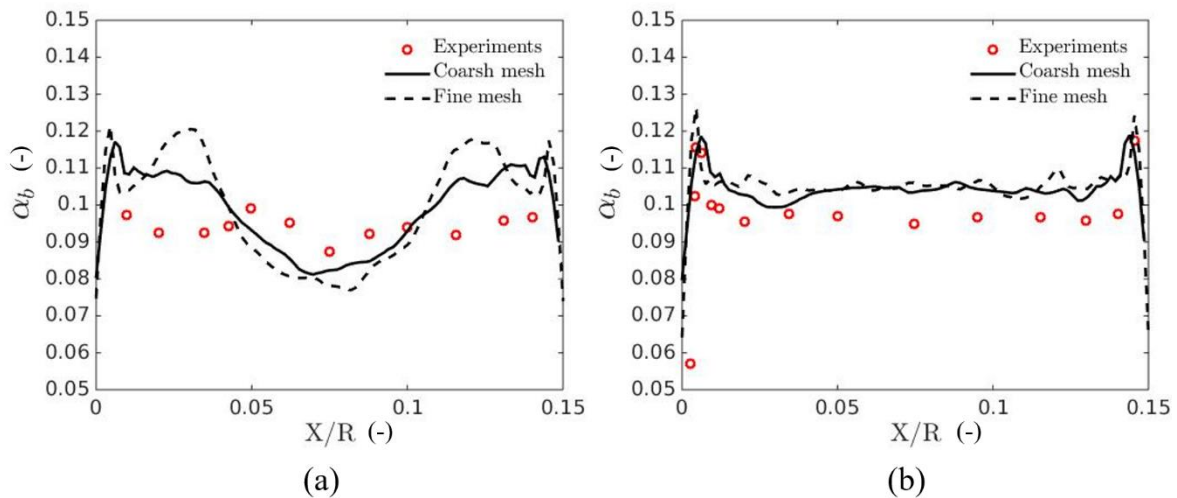


Fig. 40. Comparison of the time averaged air volume fraction simulations (coarse and fine mesh) with experiments over $t = 70$ s at a height of (a) 0.07 and (b) 0.15 m.

Table 20. The RMS values for the time averaged volume fraction simulations for coarse and fine mesh sizes at different heights and over $t = 70$ s.

Vertical Location (m)	RMS $(\alpha_g)_{\text{coarse}}$ (-)	RMS $(\alpha_g)_{\text{fine}}$ (-)
$z = 0.05$	0.014	0.018
$z = 0.7$	0.013	0.017

In the experiment, the time averaged air volume fraction was smoother than the results observed in the simulations, which predicted significant oscillations near the inlet region (Fig. 39 and Fig. 40 (a)). However, both the experiments and the simulations showed a similar trend at $z = 0.07$ m. The maximum Stokes number ($St_{\text{max}} = 0.032$) in this simulation was far less than one, which indicates that the fluid drives the bubble motion, since the bubbles rapidly adapt to the liquid velocity field (Passalacqua et al., 2010). Fig. 41 shows the mean liquid velocity vector field.

In Fig. 41, there is liquid downflow near the wall. Four giant vortexes form in the liquid flow near the bottom of the bubble column and a higher liquid velocity is observed in the flow near the inlet area. Since bubbles quickly adapt to the liquid velocity, more air flows between the vortexes (red line in Fig. 41). Thus, the air flow near the center of the inlet region is less intense. Near the inlet location, the time averaged air volume fraction at $z = 0.07$ m in Fig. 39 and Fig. 40 shows a high volume fraction near the wall and low volume fraction in the center. At higher locations, the air was more uniformly distributed.

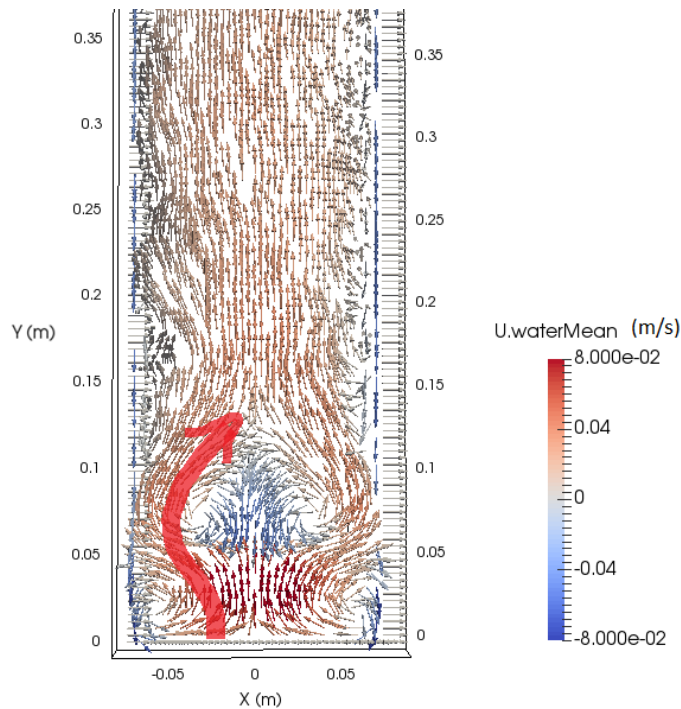


Fig. 41. Comparison of the time averaged liquid velocity vectors over $t = 70$ s near the inlet location.

In summary, both the coarse and fine mesh simulations provided good results compared to the Hartevelde (2005) experimental data, but were not accurate near the inlet location. At the higher regions of the bubble column, where $z = 0.15$ m, the simulation results were in good agreement with experimental data. Overall, according to this mesh convergence test, the coarse mesh would be a good selection for further simulations for this bubble column, because the calculation time is lower compared to the finer mesh case and the prediction result remained reasonable.

4.3. Stability Analysis of the Cylinder Bubble Column

In this section, the stability analysis of the flow for this 3D cylindrical bubble column will be discussed. It is worth noting that this stability is not the numerical stability of the calculation, but rather the stability of the physical flow. The objective of this study was to determine the inlet superficial air velocity at which stable, nearly uniform flow transitions to fully unstable, non-uniform flow patterns in the column according to the predictions of the two-fluid model.

4.3.1. Experimental overview of the cylinder bubble column stability

Harteveld (2005) investigated the transition in the bubble column by testing different inlet gas velocities, as shown in Table 21 for the uniform air injection condition (C1). The experiments showed that large structures occurred at injection gas velocities of approximately 0.047 m/s. At this velocity, wall peaks in the gas volume fraction also appeared for all the height locations.

Table 21. Superficial gas velocities for different gas fractions (Harteveld, 2005).

U_g (m/s)	α (Gas Volume Fraction)	Number of Needles
0.015	6.1%	187
0.017	7.6%	187
0.025	11%	187
0.032	16%	559
0.039	20%	559
0.049	25%	559

4.3.2. Cylinder bubble column stability analysis in OpenFOAM

The flow stability was investigated computationally using the same numerical setup described previously for the cylindrical bubble column, along with a bubble diameter of 4 mm. The two-fluid model was the base model for calculations in OpenFOAM and the sub-models applied to this simulation were the same as the mesh convergence test (section 4.2).

Table 22 provides the various simulated superficial gas velocities with the corresponding initial water levels to match the Hartevelde (2005) experimental setup.

Table 22. Superficial gas velocities for different gas fractions (OpenFOAM simulations).

U_g (m/s)	Initial Water Level (m)
0.015	1.3
0.025	1.3
0.032	1.3
0.039	1.3
0.049	1.3
0.076	1

The boundary conditions for this cylinder bubble column are shown in Table 18 in section 4.2, in which B1 is the bottom plane (i.e., the air injection area), B2 is the wall, and B3 is the outlet, which is open at the top. The only differences between the cases are the initial water level and the inlet gas velocity

The results for the first case with a superficial gas velocity of $U_g = 0.015$ m/s are shown in Fig. 42, which reports the time averaged volume fraction over $t = 50$ s at different locations, in

which the horizontal axis of the figure corresponds to the normalized axis of the bubble column, with 0 indicating the location at the center of the column, and 1 denoting to the location of the wall. The vertical axis shows the time averaged volume fraction.

All of the OpenFOAM simulations at these conditions, except at a height of $z = 0.07$ m, showed uniform air flow and trended well with the experimental results (Fig. 42). These simulations even predicted the same wall peaking observation as the experimental result at a horizontal normalized location of 0.9–0.95. All the simulations tended to show higher time average volume fraction values compared to the experimental results, but the difference was not significant. For example, simulations calculated a time averaged air volume fraction of around 7%, while the experimental results gave a value of approximately 6%. However, no simulation predicted results similar to the experiments at a horizontal normalized location of 0.95–1 (i.e., the wall).

At a height of $z = 0.07$ m, the OpenFOAM simulation did not provide a very uniform air distribution compared with the experimental result. Instead, the simulation showed there were fewer bubbles in the center of the column, but more air flow off-center. This deviation probably happened due to the selection of the lift sub-model, which tends to put more bubbles pushing toward the wall. Overall, at this superficial gas injection velocity, the simulation provided a good prediction of the experimental results.

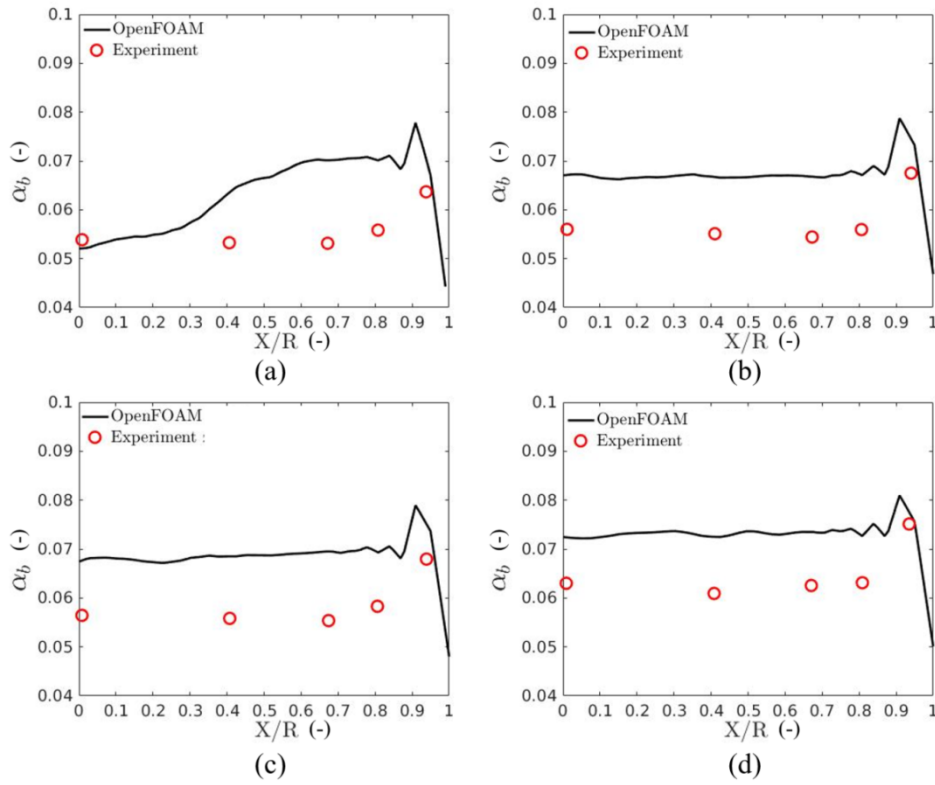


Fig. 42. Time averaged air volume fraction simulations and experiments at a superficial gas velocity of $U_g = 0.015$ m/s and different height locations in the bubble column, including (a) 0.07 m, (b) 0.3 m, (c) 0.6 m, and (d) 1.2 m.

Fig. 43 shows the time averaged air volume fraction of the cylinder bubble column at different heights using a slightly faster superficial gas velocity of $U_g = 0.049$ m/s. At this velocity, the time averaged air volume fractions between the OpenFOAM simulations and experimental results were similar ($\sim 25\%$). Both sets of tests showed the small peak in the profile near the wall, but experimentally this phenomenon actually happened closer to the wall than the simulations suggested. In addition, the simulations appeared more uniform compared with the experimental results at this velocity. In the experiment at a height of $z = 0.15$ m, the time average air volume fraction profile drops near the wall area due to the wall lubrication force that drives

bubble away. In simulations, this effect is described by Antal et al. (1991), and accordingly the simulation profiles demonstrated a drop in the air volume fraction at the wall.

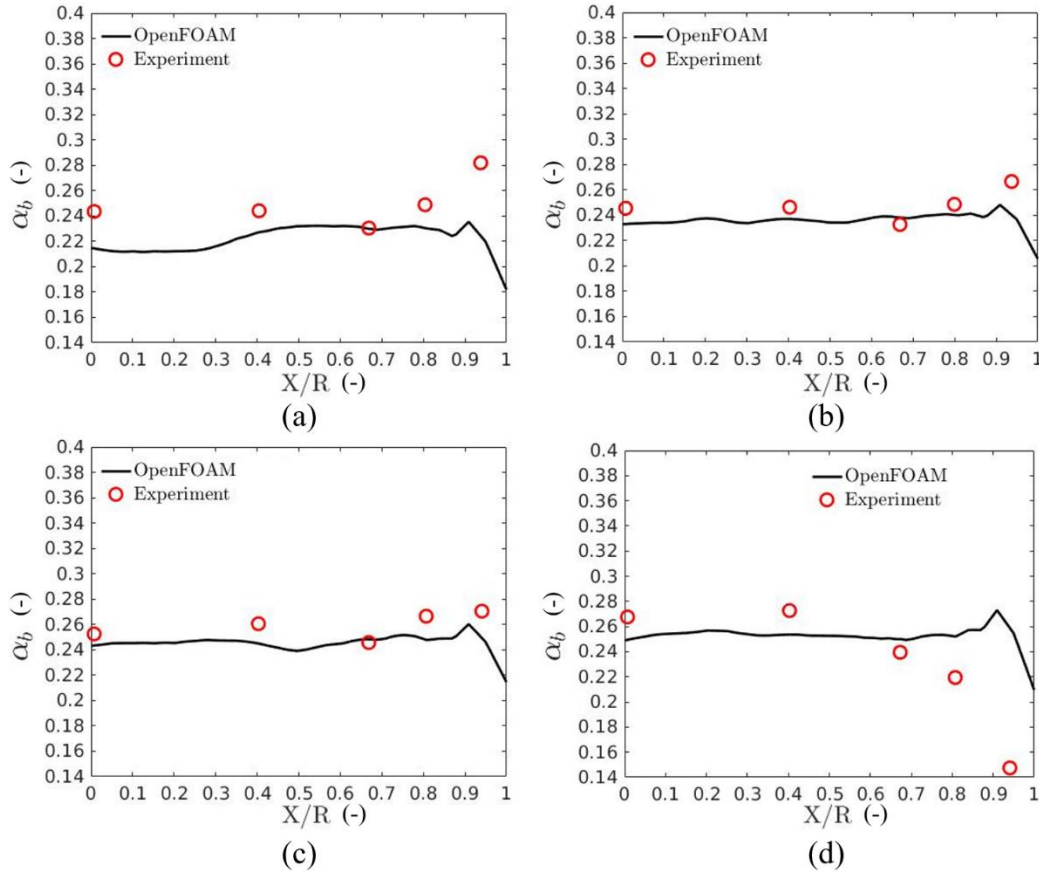


Fig. 43. Time average air volume fraction simulations and experiments with a superficial gas velocity of $U_g = 0.049$ m/s at different heights of (a) 0.08 m, (b) 0.3 m, (c) 0.8 m, and (d) 1.5 m.

Fig. 44 shows the simulated and experimental time averaged air volume fraction profiles for superficial gas velocities that ranged from 0.015 m/s to 0.049 m/s at a height of $z = 1.2$ m. According to the plots, both the simulation and experimental results did not show any large scale structures, rather the bubble columns showed highly uniform flow for different superficial velocities. Hartevelde (2005) mentioned that in the experiment at $\alpha = 25\%$ and at this height, the void fraction was not very uniform, and at low superficial gas velocities, the wall peaking behavior

disappeared at higher locations. Also, the author observed a small dip behavior after the superficial gas velocity reached $U_g > 0.032$ m/s.

In the simulations, the results matched Hartevelde (2005) very well at a height of $z = 1.2$ m, even though the time averaged air volume fraction values matched the experimental values. All simulation results showed a wall peaking and dipping behavior between the normalized horizontal locations of 0.9–1, which happens due to the wall lubrication force. The stability analysis for the superficial gas velocities from 0.015 m/s to 0.049 m/s was in very good agreement with the experimental results; no large scale was observed.

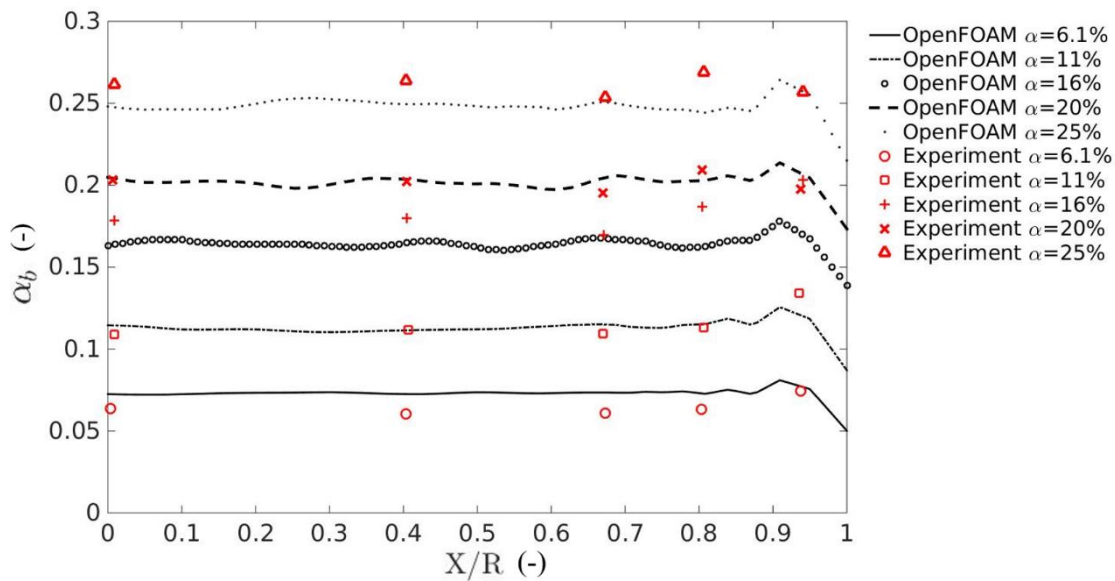


Fig. 44. The simulated and experimental time averaged air volume fractions at a height of $z = 1.2$ m and superficial gas velocities that ranged from 0.015 m/s to 0.049 m/s. The global void fraction was 6.1% to 25%.

In Hartevelde's (2005) experiment, the largest superficial gas velocity tested was $U_g = 0.076$ m/s at an initial water level of 1 m. For this scenario, a large-scale dynamic structure appeared and bubbles peaked at the center of the column, which is shown in Fig. 45 along with the corresponding simulations.

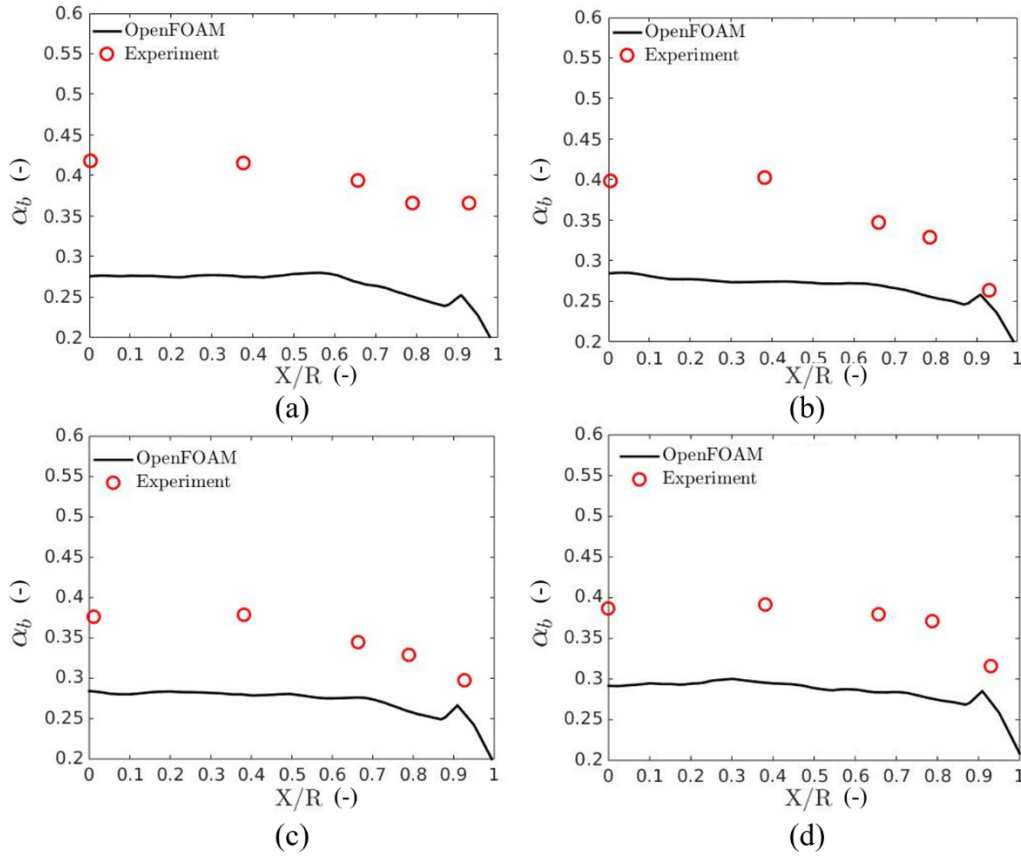


Fig. 45. Simulated and experimental time averaged air volume fractions with a superficial gas velocity of $U_g = 0.076$ m/s at different heights, including (a) 0.15 m, (b) 0.3 m, (c) 0.6 m, and (d) 1.16 m.

The results of the simulations at $U_g = 0.076$ m/s were very different from the experimental data. The time averaged air volume fraction profile for the OpenFOAM simulation was 29%, but the corresponding Harteveld (2005) experimental result was around 40%. Also, in the experiment, there was obvious center peaking behavior, but while the simulation showed a central peak in the time average air volume fraction, it was not as obvious as the experimental result. Furthermore, in the experiment, there was no wall peaking behavior observed, however in the simulation at a normalized location of approximately 0.9 we can observe a small degree of peaking behavior. If there was no measurement error for the Harteveld result at this velocity, then we

can conclude that the OpenFOAM simulation prediction for this high superficial gas velocity does not provide a very accurate result, but only shows the trend of the flow behavior.

The axial normal stress of the liquid velocity in a bubble column can be a very useful value for studying the distribution of large scale structures in the vertical direction. Fig. 46 shows a comparison of the simulated and experimentally measured axial normal stress of the liquid velocity as a function of the height at the normalized location of 0.82. The horizontal axis of the figure is the normalized height of the bubble column, and the vertical axis is the axial normal stress. From this figure, we can see that below 39% ($U_g = 0.066$ m/s) of the air volume fraction, the simulation results were in good agreement with the experimental results, but at $U_g = 0.076$ m/s, the damping of the axial normal stress was very high, though the simulation showed a similar downward trend as the experimental axial normal stress profile. This means, the fluctuation of the bubbly flow at this velocity was very high.

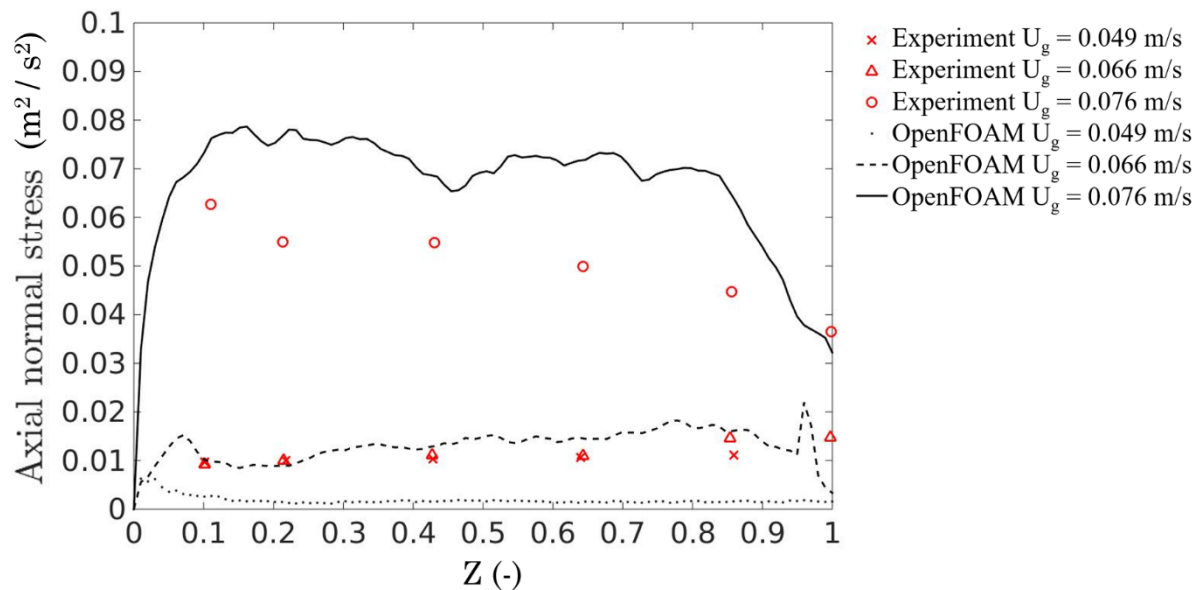


Fig. 46. Simulated and experimental results of the axial normal stress of the liquid velocity as a function of the height at the normalized location of 0.82.

4.3.3. Conclusion

In summary, the OpenFOAM simulations were in very good agreement for both the time averaged profiles and trends of the Harteveld experimental results for the 3D cylinder bubble column. The grid size for the simulations was 4 mm, which can be the same as the bubble size. The prediction of the two-fluid model can provide accurate results compared with the experiment, especially for superficial gas velocities below $U_g = 0.049$ m/s ($\alpha = 25\%$). When the superficial gas velocities were greater than this value, the simulation predictions provided appropriate trends of the flow behavior, but the error of numerical results increased. For example, at a superficial gas velocity of $U_g = 0.076$ m/s, the error between the simulation and experiment was about 20%. Near the inlet area, the simulation results showed some error compared with the Harteveld (2005) experimental results, which was probably due to the choice of sub-models for the wall lubrication and virtual mass forces. Moreover, it may be worthwhile changing the lift force model to the Tomiyama lift model, since the cylinder bubble column behaves more like a pipe flow.

Overall, the two-fluid model in OpenFOAM provided very accurate predictions, and with the correcting settings (e.g., raise velocity, bubble diameters, etc.), geometry, and scale it is possible these predictions can be used by industry.

4.4. Validation of Bubble Dispersion Force in the Two-Fluid Model

In the previous section, the two-fluid model was validated and provided a physical stability analysis for a cylindrical bubble column based on the experimental work of Harteveld (2005). Overall, the time averaged results from the two-fluid model provided good trends with the experimental data, both at the center and close to the walls of the bubble column. For superficial gas injection velocities between 0.015 m/s to 0.049 m/s, the simulated time averaged air volume

fraction profile at higher locations was in good agreement compared with the experimental results. However, near the injection region, the simulation of the time averaged air volume fraction at those velocities did not match the experiment well, probably due to the selection of the sub-models, such as the virtual mass force, which will have a strong impact when the bubbles are accelerating near the inlet region. For a higher superficial gas injection velocity (0.076 m/s), the simulated global air volume fraction did not match with the experimental results. Additionally, the physical stability of the bubble column happened earlier in simulation than in the corresponding experiments. In the simulations, the instability occurred around 0.03 m/s, but in the Harteveld (2005) experiment, a large dynamic structure happens at a superficial gas velocity around 0.05 m/s. Therefore, in this section, by adding the bubble dispersion force into the two-fluid model in order to study how the physical stability of the system is affected when the concentration of the bubbles is higher or the injection superficial gas velocity is greater.

4.4.1. Case setup

A few different case studies were studied in order to complete the validation of the influence of the bubble dispersion force on the two-fluid model. First, the cylindrical bubble column at a range of superficial gas velocities would be tested, from 0.39 m/s to 0.49 m/s, since the simulation results already shown that low superficial gas velocities without bubble dispersion are in good agreement compared with the Harteveld (2005) experimental results. However, the simulation of the cylindrical bubble column without bubble dispersion force at the highest superficial gas injection velocity (0.076 m/s) did not agree very well with the experiment due to the higher gas concentration. Therefore, it was important to validate the bubble dispersion force in the two-fluid model at this higher superficial gas injection velocity of 0.076 m/s.

Second, a validation of the non-uniformed aeration condition was performed for the rectangular bubble column using bubble dispersion force, and compared the results based on Pflieger et al., 1999.

4.4.2. Cylindrical bubble column analysis

In order to study the effects of the bubble dispersion force on my simulations, the same geometric dimensions was used for the cylindrical bubble column as discussed in previous sections (diameter = 0.15 m, height = 2 m), and a constant bubble injection diameter of 4 mm. The average grid size of the simulation mesh was 4 mm. Three injection velocities were validated for this system, which are shown in Table 23.

Table 23. Superficial gas velocities for different gas fractions (OpenFOAM simulations).

U_g (m/s)	Initial Water Level (m)
0.039	1.3
0.049	1.3
0.076	1

As described in previous sections, the two-fluid model was used to solve the system in conjunction with various sub-models, including the Tomiyama drag model (Tomiyama et al., 1998), the Legendre and Magnaudet lift model (1998), the Antal wall lubrication model (Antal et al., 1991), and a constant virtual mass coefficient (Drew, 1979) to account for momentum exchanges between phases.

Fig. 47 shows the instantaneous air volume fraction for three different injection velocities both with and without the bubble dispersion force add-in. With the bubble dispersion force, the

air volume fraction diffused uniformly along the column for superficial gas velocities of 0.039 m/s and 0.049 m/s compared to the results without the bubble dispersion force, which resulted in the formation of a large dynamic structure. For the superficial gas injection velocity of 0.076 m/s, both cases with and without the bubble dispersion force became unstable, with large dynamic structures appearing. All three injection velocity simulation results with bubble dispersion were in agreement with the Harteveld (2005) experimental results.

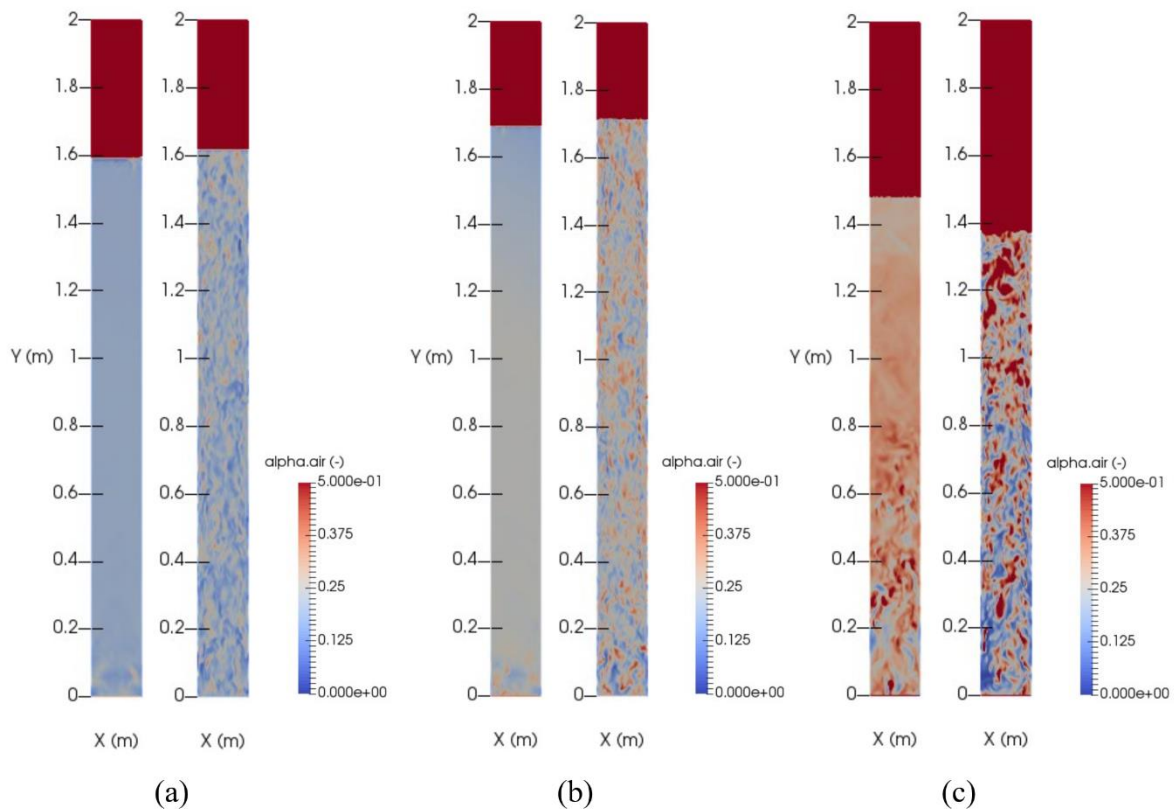


Fig. 47. A comparison of the instantaneous air volume fraction for three different injection velocities, including (a) 0.039 m/s, (b) 0.049 m/s, and (c) 0.076 m/s, both with (left) and without (right) the bubble dispersion force model.

A comparison of the time averaged air volume fraction results between simulations run with and without the bubble dispersion force for the superficial gas velocity of 0.039 m/s is shown in Fig. 48, in which the results with the bubble dispersion force were very flat along that location, which means the bubbles were uniformly distributed. However, without the bubble dispersion force, the time averaged result was actually in more agreement with the experimental results.

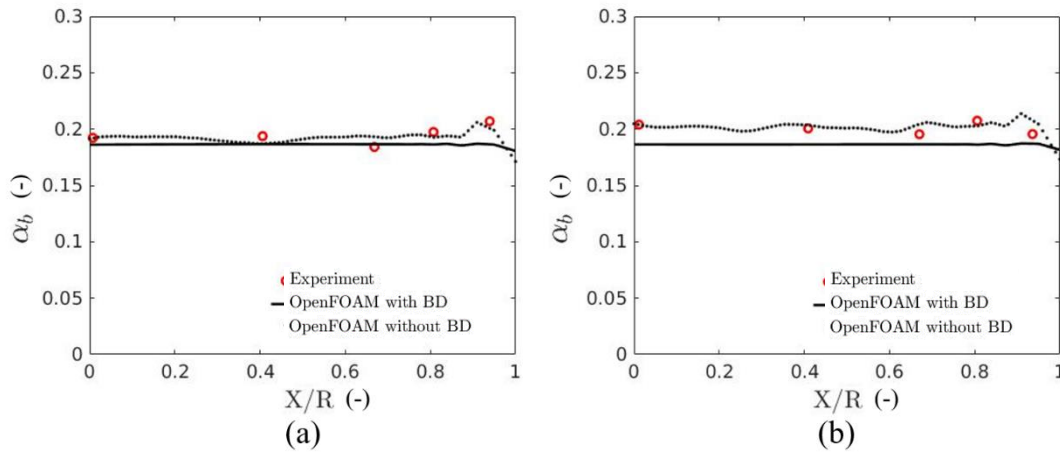


Fig. 48. Comparison of the time averaged air volume fractions for experiments and simulations both with and without the bubble dispersion (BD) force for a superficial gas velocity of 0.039 m/s at different vertical locations, including (a) 0.6 m and (b) 1.2 m.

Fig. 49 shows a comparison of the time averaged air volume fractions for a higher air injection velocity of $U_g = 0.049$ m/s. In the Hartevelde (2005) results, the author measured the global air volume fraction to be around 25% at this air injection velocity. At a height of $z = 0.08$ m, the simulation results both with and without the bubble dispersion force showed a similar trend as the experimental results. However, at a higher location in the bubble column ($z = 1.5$ m), both cases did not match the time averaged air volume fraction profile of the experimental results, which is probably due to the lift force effect, in which more bubbles tend to be pushed

toward the wall. Therefore, the observation shows the simulated time averaged air volume fraction profile near the wall at $z = 1.5$ m was higher than the experimental data at these conditions, whether or not the bubble dispersion force was used.

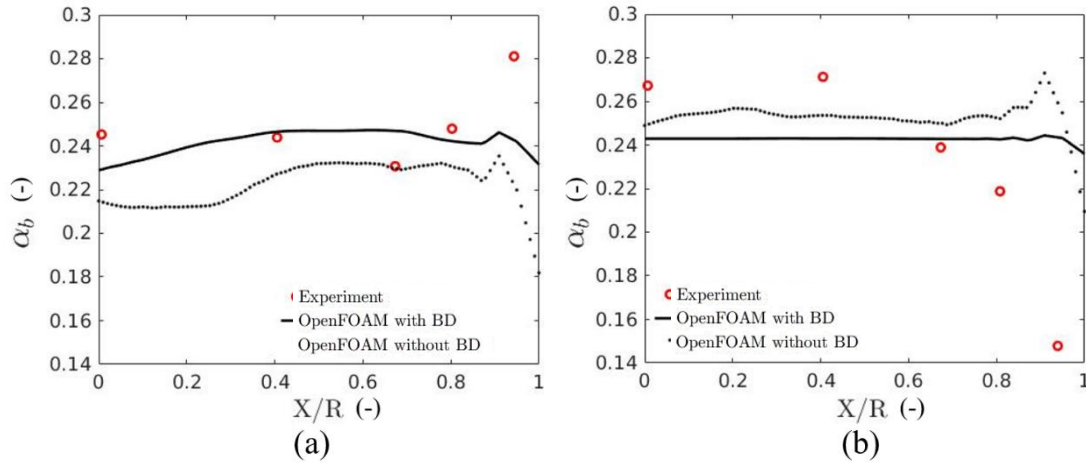


Fig. 49. Comparison of the experimental and simulated time averaged air volume fractions both with and without the bubble dispersion (BD) force for a superficial gas velocity of 0.049 m/s at different vertical locations, including (a) 0.08 m and (b) 1.5 m.

Fig. 50 provides a comparison of the time averaged air volume between the simulations run with and without the bubble dispersion force for a superficial air injection velocity of $U_g = 0.076$ m/s. In this comparison, both simulation results predicted less gas compared with the experimental data for the global air volume fraction. The results with the bubble dispersion force showed some advantage over the results without bubble dispersion, featuring less waviness in the profile compared to the results produced without the inclusion of the bubble dispersion force. This difference is likely due to the diffusivity term in the expression of the bubble dispersion force, which is described in Chapter 2.

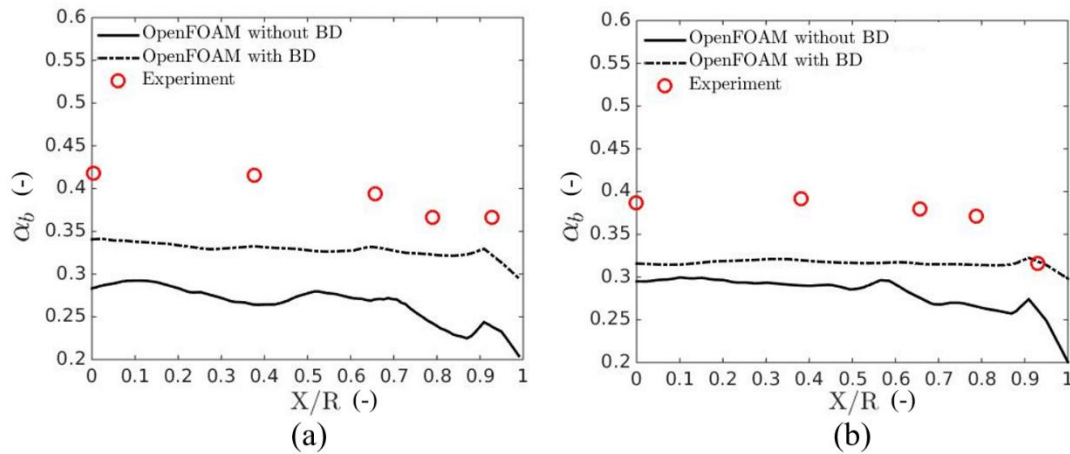


Fig. 50. Comparison of the time averaged air volume fraction experimental results and simulations performed with and without the bubble dispersion (BD) force for a superficial gas velocity of 0.076 m/s at different vertical locations, including (a) 0.15 m and (b) 1.16 m.

Fig. 51 shows the time averaged liquid axial velocity profile for a gas injection superficial velocity of 0.076 m/s. At this velocity, the liquid axial velocity profile with the bubble dispersion force provided strong agreement with experimental data at the lower height of $z = 0.15$ m. However, at the higher location of $z = 0.9$ m, the results of the simulation without the bubble dispersion force showed a better fit with the experimental data. The simulation with the bubble dispersion force at $z = 0.9$ m only matched the experimental data points near the wall, which supports Hartevelde's (2005) findings that the liquid velocity close to the wall is relatively small in comparison with the center velocity of the column.

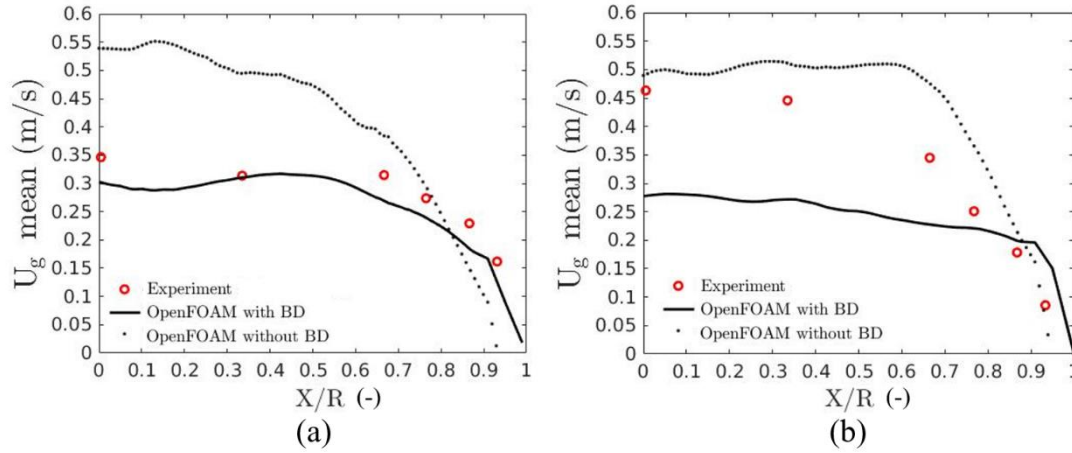


Fig. 51 Comparison of the time averaged gas axial velocity experiments and simulations both with and without the bubble dispersion (BD) force at a superficial gas velocity of 0.076 m/s at different vertical locations in the column, including (a) 0.15 m and (b)

4.4.3. Validation of the bubble dispersion force for the Pflieger case

All the cylindrical bubble column simulations were tested with a uniform aeration gas injection pattern from the inlet. However, a non-uniform aeration (Pflieger et al., 1999) bubble column remains to be validated for the proposed two-fluid model. Pflieger et al. (1999) constructed a rectangular bubble column with a non-uniform air injection pattern at the inlet, which is shown in Fig. 52. This bubble column was 0.2 m in width, 0.8 m tall, and 0.05 m in depth. Its initial water level was 0.45 m. The inlet area was 0.01 m in width and 0.05 m in depth, and was located at the center gap of the bottom of the bubble column. The standard flow rate for the air injection was around 48 L/h. The authors used LDA to measure the velocity.

For the simulation of the Pflieger case (Pflieger et al., 1999), a non-constant bubble diameter is assumed, in which the initial diameter of the bubble was 2 mm and changed as a function of its height in the liquid. The grid size was set to a uniform value of 4 mm (for a grid of 28×200×12 cells) and fully calculated the simulation in 3D. As described in previous sections,

the two-fluid model was used to solve the system, along with the Tomiyama drag model (Tomiyama et al., 1998), the Legendre and Magnaudet lift model (1998), the Antal wall lubrication model (Antal et al., 1991), a constant virtual mass coefficient (Drew, 1979), and an additional bubble dispersion force term. The boundary conditions for the Pfleger case (Pfleger et al., 1999) are shown in Table 24, in which B1 was the inlet located on the bottom of the bubble column, B2 was the wall surface for all 4 sides (left, right, front and back), and B3 was the outlet on the top of the bubble column, which was open to the atmosphere.

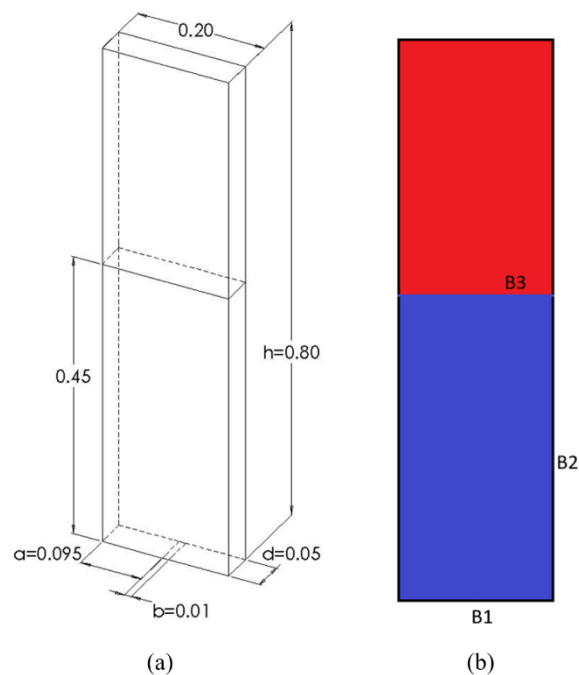


Fig. 52. The Pfleger bubble column overview and dimensions (Pfleger et al., 1999). The blue-shaded area is the liquid phase and the red-shaded area is the gas phase.

Table 24. Boundary conditions.

BC	Bubble Phase	Liquid Velocity	Liquid Pressure
B1 Inlet	Fixed Value	Fixed Value	Zero Gradient
B2 Wall	Zero Gradient	No Slip	Zero Gradient
B3 Outlet	Zero Gradient	Zero Gradient	Fixed Value

Fig. 53 shows the experimental results and simulations of the instantaneous air volume fraction at $t = 4$ s, both with and without the bubble dispersion force. At the beginning of the gas injection for the simulation with the bubble dispersion force, the instantaneous air volume fraction profile was more stable and did not show fluctuation. However, for the simulation without the bubble dispersion force term, the volume fraction started to fluctuate early (around $t = 4$ s), and this fluctuation became stronger as time increased, which is shown in Fig. 54. This result confirms that the bubble dispersion force could help the physical stability in the two-fluid model.

Fig. 55–57 show the comparison of the time averaged liquid axial velocity between the experimental and simulated results at different locations in the bubble column. Near the wall region, the simulated liquid velocity was negative, which was in good agreement with the experimental flow behavior. From this comparison, the time averaged profiles do not show a major effect on both the results with and without the bubble dispersion force due to the low flow rate.

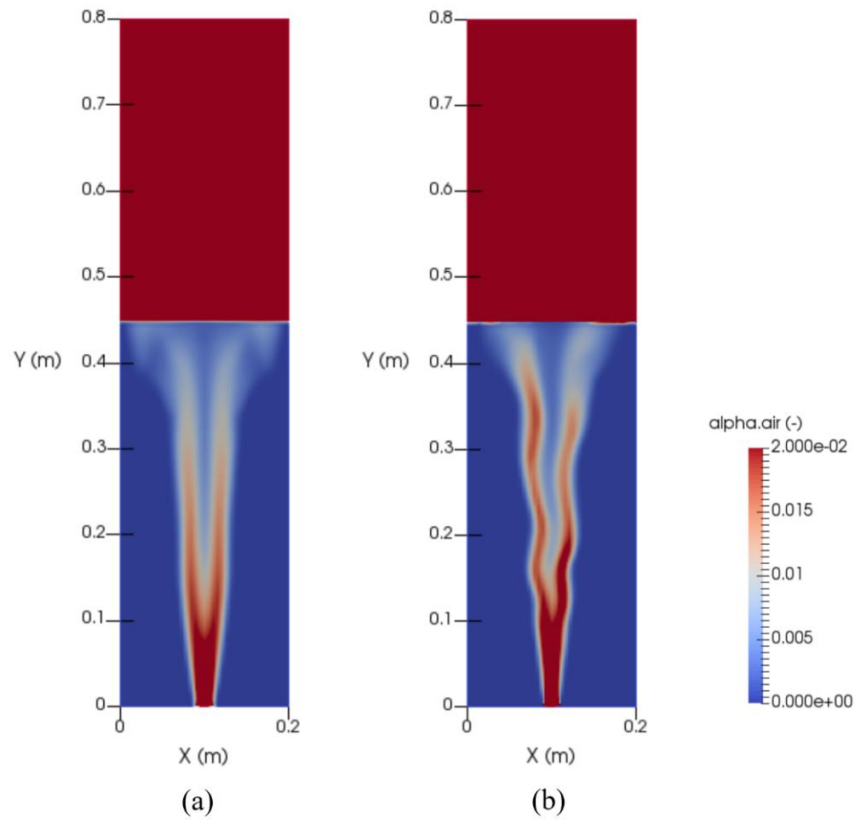


Fig. 53. Comparison of the simulated instantaneous air volume fraction at $t = 4$ s (a) with and (b) without the bubble dispersion force.

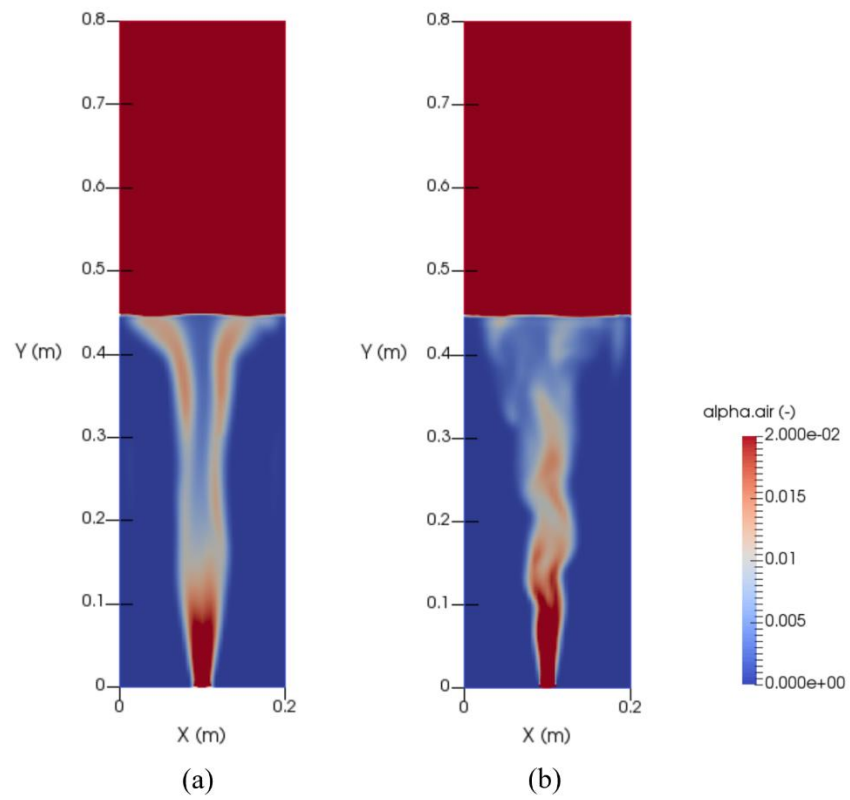


Fig. 54. Comparison of the simulated instantaneous air volume fraction at $t = 7$ s, (a) with and (b) without the bubble dispersion force.

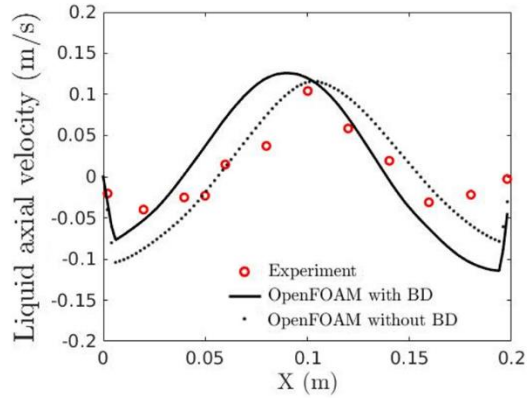


Fig. 55. Comparison of the experimental and simulated time averaged liquid axial velocity profiles both with and without the bubble dispersion (BD) force for a height of $z = 0.13$ m.

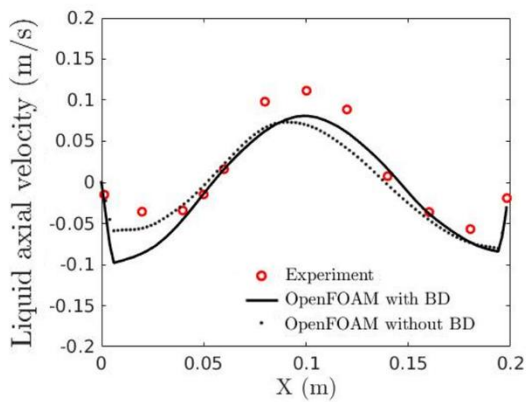


Fig. 56. Comparison of the experimental and simulated time averaged liquid axial velocity profiles both with and without the bubble dispersion (BD) force for a height of $z = 0.25$ m.

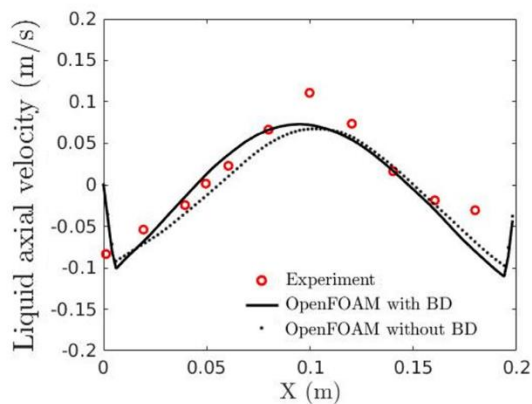


Fig. 57. Comparison of the experimental and simulated time averaged liquid axial velocity profiles both with and without the bubble dispersion (BD) force for a height of $z = 0.37$ m.

4.4.4. Conclusion

For a cylindrical bubble column, the time averaged profiles predicted by the two-fluid model without the bubble dispersion force term trended well compared with the experimental results and were in good agreement with the experimental data when the air injection velocities were between 0.015 m/s and 0.049 m/s. With higher injection velocities, such as 0.076 m/s, the time averaged result of the two-fluid model without the bubble dispersion force did not agree very well with the experimental result.

Also, the flow stability analysis results did not show the same predictions as Hartevelde (2005) in cases without the bubble dispersion term. The instability was observed in the simulation even with low air injection velocity, starting around 0.03 m/s. However, Hartevelde (2005) observed instability in the bubble column starting around 0.05 m/s. With the bubble dispersion force, at low air injection velocities ranging from 0.015 m/s to 0.049 m/s, the time averaged result did not change significantly, but there was a reduction in the oscillations of the time averaged air volume fraction profile. For higher gas injection velocities (0.076 m/s), the time averaged profiles from the simulations partially fit the experimental data. In terms of the flow stability analysis, with the bubble dispersion force the prediction did not show large dynamic structures for an injection velocity of 0.05 m/s due to the added effect of the bubble dispersion force term, which is in agreement with the experimental results of Hartevelde (2005).

In the Pflieger et al. (1999) validation test case, no major effects of the bubble dispersion force were observed on the time-averaged profiles. The overall effect of the bubble dispersion force was to stabilize the flow, which can be explained by the fact that this term tends to make the gas volume fraction more uniform. Its effect is more evident in cases where there is a high gradient in the volume fraction.

CHAPTER 5. CONCLUSION

The goal of this thesis was to gather a detailed understanding of the two-fluid model for the simulation of gas-liquid flows. A detailed study was performed using the open source software OpenFOAM, which enabled to investigate and determine the effects of drag, lift, virtual mass, and wall lubrication forces on the simulation of bubbly flows. With this work, an accurate simulation of the flow behavior inside a bubble column is very success. By testing different column configurations and superficial gas injection velocities, the investigation of the dynamic large-scale fluctuations that characterize flow in a bubble column can be accomplished.

5.1. Investigating the 2D Rectangular Bubble Column

In this work, a pseudo 2D bubble column (Harteveld, 2005) was simulated that incorporated the Tomiyama drag law (Tomiyama et al., 1998) and the Legendre and Magnaudet lift model (Legendre and Magnaudet, 1998), since they provided satisfactory results in agreement with the experiments considered in the preliminary model tests. The Antal wall lubrication model (Antal et al., 1991) and a constant virtual mass coefficient equal to 0.5 (Drew et al., 1979) were selected. Both 2D and 3D simulations were performed, with improved results evident in 3D simulations compared to 2D. However, the difference in the results did not justify the additional computational cost. Therefore, 2D simulations in the remainder of the study can be performed.

5.2. Investigating the Cylindrical Bubble Column

The 3D bubble column of Harteveld (2005) was simulated as an example of the cylindrical column. Compared with the Harteveld experimental results, most of the simulations performed with the two-fluid model showed good agreement for superficial gas velocities below

$U_g = 0.049$ m/s ($\alpha = 25\%$). However, some of the details observed experimentally were not captured by the simulations, such as the gas volume fraction peak near the column wall, and the volume fraction profiles near the inlet. With higher superficial gas injection velocities, the agreement of the two-fluid model predictions with the experiments diminished further (15%–20% error compared with the experimental results). This outcome could be explained by the fact that the sub-models may not be sufficiently accurate. The experimental measurements used as reference may also have been affected by uncertainty.

5.3. Future Work

The lift force model of Tomiyama (1998), which was designed for bubbly flows, will be tested to verify if it provides a significant change in the prediction of the two-fluid model simulation near the inlet location of the bubble column since the Tomiyama correlation was specifically developed based on experiments of gas-liquid systems. Bubble dispersion will also be used as a standard sub-model in all future simulations.

REFERENCES

- Antal, S.P., Lahey, R.T., Flaherty, J.E., 1991. Analysis of phase distribution in fully developed laminar bubbly two-phase flow. *International Journal of Multiphase Flow* 17, 635–652.
- Davidson, M.R., 1990. Numerical calculations of two-phase flow in a liquid bath with bottom gas injection: The central plume. *Applied Mathematical Modelling* 14, 67–76.
- Drew, D.A., 1982. *Continuum Modeling of Two-Phase Flows*.
- Drew, D.A., Lahey, R.T., 1987. The virtual mass and lift force on a sphere in rotating and straining inviscid flow. *International Journal of Multiphase Flow* 13, 113–121.
- Drew, D., Cheng, L., Lahey, R.T., 1979. The analysis of virtual mass effects in two-phase flow. *International Journal of Multiphase Flow* 5, 233–242.
- Frank, T., Zwart, P.J., Krepper, E., Prasser, H.-M., Lucas, D., 2008. Validation of CFD models for mono- and polydisperse air–water two-phase flows in pipes. *Nuclear Engineering and Design, Benchmarking of CFD Codes for Application to Nuclear Reactor Safety* 238, 647–659.
- Harteveld, W.K., 2005. *Bubble columns: Structures or stability?* Delft University of Technology.
- Jakobsen, H.A., 2009. *Bubble Column Reactors*, in: *Chemical Reactor Modeling*. Springer Berlin Heidelberg, pp. 757–806.
- Law, D., Battaglia, F., Heindel, T.J., 2008. Model validation for low and high superficial gas velocity bubble column flows. *Chemical Engineering Science* 63, 4605–4616.
- Lee, S.L., Wiesler, M.A., 1987. Theory on transverse migration of particles in a turbulent two-phase suspension flow due to turbulent diffusion—I. *International Journal of Multiphase Flow* 13, 99–111.

- Legendre, D., Magnaudet, J., 1998. The lift force on a spherical bubble in a viscous linear shear flow. *Journal of Fluid Mechanics* 368, 81–126.
- Monahan, S.M., Fox, R.O., 2009. Validation of Two-Fluid Simulations of a Pseudo-Two-Dimensional Bubble Column with Uniform and Nonuniform Aeration. *Industrial & Engineering Chemistry Research* 48, 8134–8147.
- Moraga, F.J., Bonetto, F.J., Lahey, R.T., 1999. Lateral forces on spheres in turbulent uniform shear flow. *International Journal of Multiphase Flow* 25, 1321–1372.
- Mudde, R.F., Lee, D.J., Reese, J., Fan, L.-S., 1997. Role of coherent structures on Reynolds stresses in a 2-D bubble column. *AIChE Journal* 43, 913–926.
- Paladino, E.E., Maliska, C.R., 2011. Computational modeling of bubbly flows in differential pressure flow meters. *Flow Measurement and Instrumentation* 22, 309–318.
- Passalacqua, A., Fox, R.O., Garg, R., Subramaniam, S., 2010. A fully coupled quadrature-based moment method for dilute to moderately dilute fluid–particle flows. *Chemical Engineering Science* 65, 2267–2283.
- Pfleger, D., Gomes, S., Gilbert, N., Wagner, H.-G., 1999. Hydrodynamic simulations of laboratory scale bubble columns fundamental studies of the Eulerian–Eulerian modelling approach. *Chemical Engineering Science* 54, 5091–5099.
- Rampure, M.R., Buwa, V.V., Ranade, V.V., 2003. Modelling of Gas-Liquid/Gas-Liquid-Solid Flows in Bubble Columns: Experiments and CFD Simulations. *The Canadian Journal of Chemical Engineering* 81, 692–706.
- Sato, Y., Sadatomi, M., Sekoguchi, K., 1981. Momentum and heat transfer in two-phase bubble flow—I. Theory. *International Journal of Multiphase Flow* 7, 167–177.
- Schiller, L., Naumann, A., 1935. A drag coefficient correlation. *Vdi Zeitung* 77, 51–86.

- Spelt, P.D.M., Sangani, A.S., 1997. Properties and Averaged Equations for Flows of Bubbly Liquids. *Flow, Turbulence and Combustion* 58, 337–386.
- Tenneti, S., Garg, R., Subramaniam, S., 2011. Drag law for monodisperse gas–solid systems using particle-resolved direct numerical simulation of flow past fixed assemblies of spheres. *International Journal of Multiphase Flow* 37, 1072–1092.
- Tomiyama, A., 1998. Struggle With Computational Bubble Dynamics. *Multiphase Science and Technology* 10, 369–405.
- Tomiyama, A., Kataoka, I., Zun, I., Sakaguchi, T., 1998. Drag Coefficients of Single Bubbles under Normal and Micro Gravity Conditions. *JSME International Journal Series B* 41, 472–479.
- White, F.M., 1974. *Viscous Fluid Flow*, McGraw-Hill. ed. New York.
- Yuan, C., Kong, B., Passalacqua, A., Fox, R.O., 2014. An extended quadrature-based mass-velocity moment model for polydisperse bubbly flows. *The Canadian Journal of Chemical Engineering* 92, 2053–2066.